SERL
technical
journal

1.0

2.8   2.5

3.2   2.2

3.6

4.0   2.0

1.1

1.8

1.25   1.4   1.6

MICROCOPY RESOLUTION TEST CHART
NATIONAL BUREAU OF STANDARDS-1963

SERL
technical
journal

UNLIMITED

BR54346

D D C

Fcb 14 1977

C

UNLIMITED

Volume 26   October 1976

C O N T E N T S ⑱ DRIC

⑲ BR-54346

Closing issue of the SERL Technical Journal.

Editorial.

410059 LB

CLOSING ISSUE OF THE SERL TECHNICAL JOURNAL

On 26th March this year at Malvern, Her Majesty the Queen unveiled a plaque commemorating the amalgamation of the Royal Radar Establishment, Malvern, the Signals Research and Development Establishment, Christchurch and the Services Electronics Research Laboratory, Baldock, to form a new combined establishment to be located at Malvern and to be called the Royal Signals and Radar Establishment (RSRE). SERL is now RSRE (Baldock) and constitutes the Electron Devices Group of the Applied Physics Department of RSRE.

One consequence of the merger is that this issue of the SERL Technical Journal will be the last. Instead, our work will appear in a new house journal which will be representative of the work of the new Establishment. Recipients of the SERL Technical Journal will receive copies of the new journal.

October 1976

G P Wright
Chief Superintendent
RSRE Baldock.
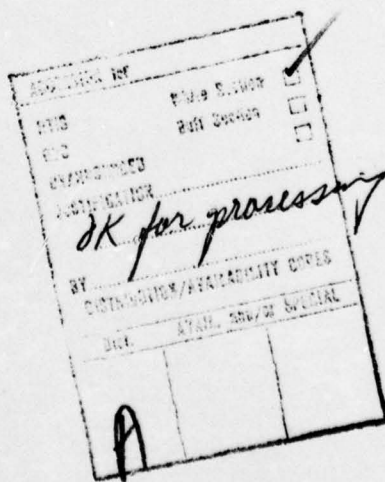
EDITORIAL

The first paper in this journal describes the design of a compact sealed waveguide CO_2 laser which has a specific output power almost a factor of two larger than previously reported. The design of these lasers depends partly on the dielectric properties of the waveguide material and whereas such data are available on single crystal material, there is little information on the polycrystalline material from which dielectric waveguides are made. The authors of the second paper have shown experimentally that the predicted power loss in hollow waveguides is material dependent and inversely proportional to the cube of the waveguide bore, and they attribute further losses to the longitudinal curvature of the waveguide and to contaminant particles in it.

The third paper is a joint one with authors from Oxford and describes work on gallium phosphide. The correlation between dark spots observed in cathodo-luminescence micrographs obtained with a scanning electron microscope, and dislocations observed in transmission electron micrographs is discussed. The authors show that the non-radiative recombination producing the dark spots is centred at dislocations and each type of dislocation has a similar effect. They suggest that the non-radiative recombination is due to the core structure of the dislocations rather than a concentration of dopant atoms or method of growth etc. The work thus gives further insight into factors affecting the efficiency of light emitting diodes.

Gallium arsenide photocathodes are the subject of the fourth paper, and here the authors discuss the reasons for the high mean transverse emission energy (MTEE) of electrons emitted from the photocathode surfaces they have developed. Lower values of MTEE would give better resolution in proximity focused devices. The authors show that the high values of MTEE can be accounted for by surface irregularities tens of nanometres in size. Further, they make an interesting comment on the use of a LEED grid assembly to analyse the angular distribution of these very low energy electrons.

There is a surfeit of published work on electron penetration into matter and the many scientists needing to know the spatial distribution of energy deposition of a bombarding beam of electrons are faced with the problem of selecting pertinent data from some scores of papers. The last paper offers a simple theory for accurately predicting 'dose-depth' curves in any medium for electron beams with kilovolt energies and above.

A. Calverley
Editor

A COMPACT SEALED WAVEGUIDE CO_2 LASER

D. R. Hall, R. M. Jenkins, E. K. Gorton and P. H. Cross

ABSTRACT

The design, construction and preliminary performance data are reported for a compact waveguide CO_2 laser which produces a high output power per unit length. The laser, of overall length 150 mm, produces 3.85 W from only 94 mm of discharge. This figure corresponds to an output power per unit length of 41 mW per mm, which is a factor of two higher than previously reported measurements. It is shown that this value is consistent with theoretical predictions based on the gain and saturation intensity measurements in the literature.

A COMPACT SEALED WAVEGUIDE CO_2 LASER

D. R. Hall, R. M. Jenkins, E. K. Gorton and P. H. Cross

1. INTRODUCTION

There have been significant advances in recent years in the development of cw waveguide CO_2 lasers[1,2,3,4]. Such lasers offer advantages over conventional CO_2 lasers, both in terms of their much larger frequency tuning range and also because of the overall reduction in size which they make possible. Suitably designed, high-pressure waveguide lasers may be used both as frequency tracking local oscillators with applications in heterodyne receivers in optical radar and communication systems, and as wide-band tunable oscillators for infra-red spectroscopy. A second class of applications, in which the laser acts as a compact source of single frequency infra-red radiation, demands a somewhat different design leading to devices which have applications as simple thermal sources (milliwatts to perhaps 10 watts), or as stable master oscillators in Doppler or F.M. ranging systems.

In this paper we describe the design, construction and preliminary performance characteristics of a waveguide CO_2 laser which has a high output power per unit length and which is suitable for use as a basic oscillator in Doppler radar systems or to provide the stable frequency input to an external amplitude or frequency modulator.

2. DESIGN AND CONSTRUCTION

In order to maximise the power output from any laser system it is necessary to minimise the so-called dissipative cavity losses which do not contribute to output coupling and the extraction of power. One such source of loss of particular importance in waveguide lasers is that associated with the propagation of the optical field within the waveguiding structure itself. Marcatili and Schmeltzer[5] have predicted that at a given wavelength, the attenuation coefficient of the fundamental EH_{11} mode which is of interest here, depends on the complex refractive index of the waveguide material and on the inverse cube of its diameter. Experimental confirmation of the general structure of this theory has recently been obtained[6], but at the time when the laser described here was constructed such experimental results were not available. However, calculations[1] based on the theory of Marcatili and Schmeltzer[5] suggested that 10 μm radiation propagation losses in straight beryllia waveguides were almost a factor of ten less than in the other candidate materials, alumina and Pyrex. On this basis and because of

the higher thermal conductivity of beryllia (which results in better discharge
cooling and hence higher optical gain), it was decided to fabricate the laser from
beryllia. Subsequent measurements[6] indicated that from the standpoint of guiding
losses alone, in waveguides with diameters larger than about 1.5 mm, both Pyrex and
alumina tubes are equally acceptable in practice (assuming they are straight) since
the losses are very small in all cases. However, the higher thermal conductivity
of beryllia, and the effect this has on gas temperature is a factor which must be
carefully assessed for optimum performance.
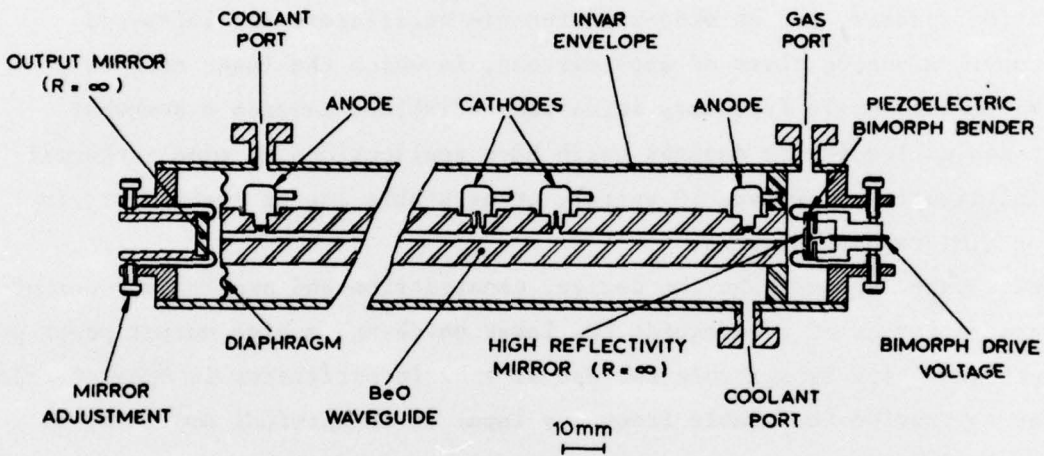
FIGURE 1. Sectional view of the sealed waveguide laser.
(Over-all length - 250 mm).

The overall laser design is shown in Figure 1. The tube used for the con-
struction of the laser was fabricated from a 99.5 per cent pure beryllia rod
129 mm in length and has a drilled bore of 2.25 mm. A four-electrode geometry is
employed with holes drilled into the bore providing a total of 94 mm discharge
length, the electrical connections to the laser being made through the end
flanges. The cavity mirrors are separated from each other by the Invar cylinder
so that the precise passive resonator length is effectively decoupled from any
thermally induced waveguide length changes. The laser is cooled by flowing an
insulating fluorocarbon fluid through the region between the waveguide and the
Invar envelope. (The measured attenuation coefficient for this waveguide tube

The mirror at the rear (non-output) end of the laser is mounted on a piezo-electric bimorph bender[7]. This device consists of two 0.25 mm thick discs of lead zirconate titanate which are oppositely poled and bonded together. A more detailed view of a bimorph bender in its mount is shown in Figure 2. The 10 mm diameter disc is constrained around an annulus by a pair of knife edges and when a voltage is applied between its two faces, a slight buckling effect is translated into linear axial motion at right angles to the disc face. To assess the dependence of mirror translation on applied voltage we placed a bimorph mount similar to that shown in Figure 2 in one arm of a Michelson interferometer and measured the displacement obtained as a function of applied voltage, diameter of the bimorph and the torque applied between the knife edges.
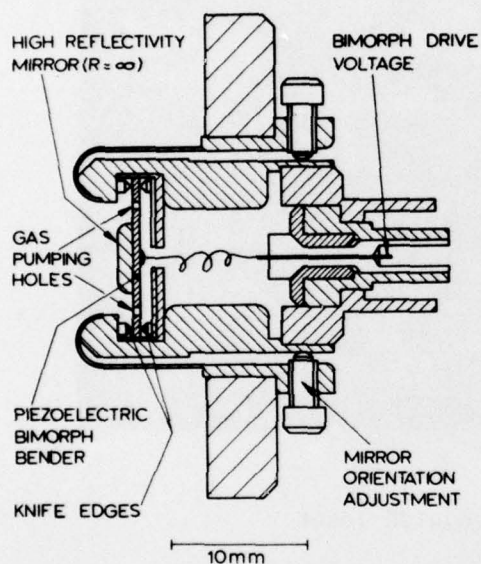
FIGURE 2. Bimorph bender mirror mount.
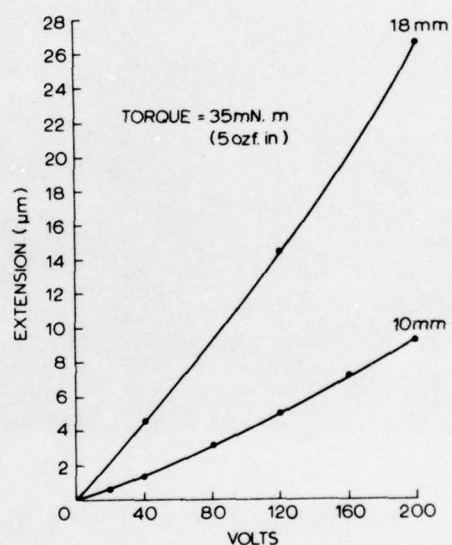
FIGURE 3. Dependence of bimorph bender translation on voltage and diameter.

The displacement produced increases fairly linearly with voltage as shown by the results in Figure 3, which were obtained using a standard 25 mm mount (18 mm bimorph) and the mount shown in Figure 2 (10 mm bimorph). The effect of increasing the torque on the retaining rings, so as to clamp the bimorph more tightly between the knife edges, is to cause a reduction in the displacement produced by a given applied voltage. We have observed this fall-off over the range 35 mN.m (5 ozf.in) (which is near the minimum required for a stable mounting) to 283 mN.m (40 ozf.in).

1.5

In addition to its much smaller size, a bimorph bender offers a major advantage over the more generally used crystal stacks because of its greatly increased displacement per volt. With the smaller disc we can obtain displacement over a full free spectral range of the laser cavity (5.3 μm) with the application of only 150 V. This compares very favourably with the applied voltages of a few kilovolts necessary with piezoelectric crystal stacks.
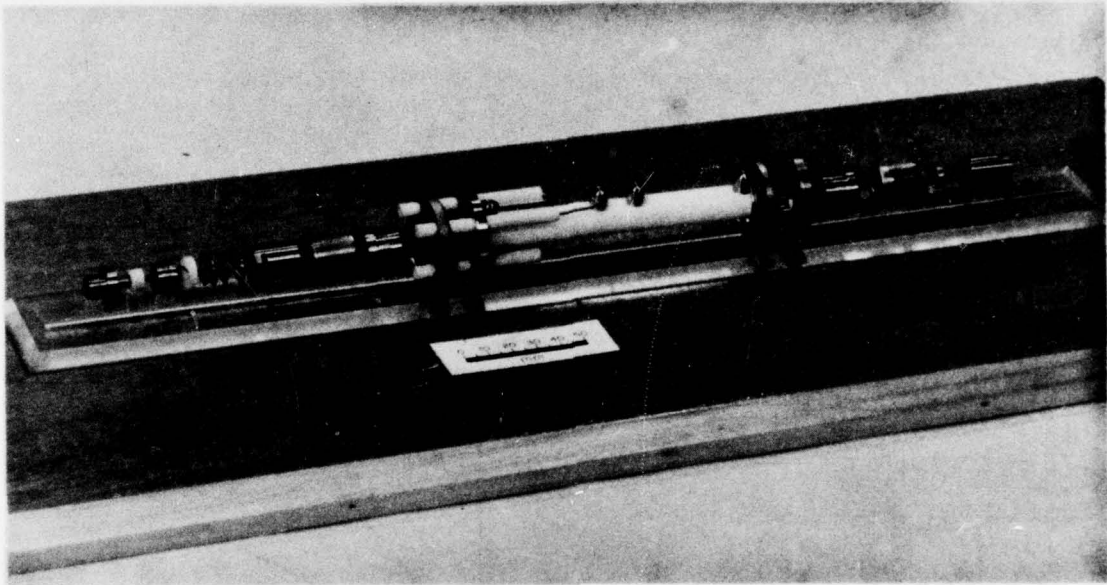
FIGURE 4. Exploded view of sealed waveguide laser.

In the mount shown in Figure 2, angular displacement of the mirror of plus or minus several tens of milliradians about each of the perpendicular axes may be achieved using the four tuning screws which bear on machined flats, using the slight flexibility of the mount. We have used a number of different mirrors as described later. In each case the mirror is epoxy-bonded to the centre of the piezoelectric disc. The output mirror is positioned in a somewhat similar mount as shown in Figure 1 and an exploded view of the whole laser is shown in the photograph in Figure 4.

3. LASER PERFORMANCE CHARACTERISTICS AND DISCUSSION

Measurements have been made of the output power of the laser under a variety of conditions of gas mixture, gas pressure, discharge current and choice

FIGURE 5. Variation of laser output power with
discharge current and pressure.

of mirror reflectivities. Most of our measurements have been made with a four-component mixture of He, CO_2, N_2 and Xe in the ratio 16:4:2:1. Figure 5 shows the variation of output power (measured with a Coherent Radiation Inc Model 210 power meter) with current for total gas pressure in the range of optimum output of 5.3 to 16 kPa (40-120 Torr). The optics used in this case were a 5 mm diameter mic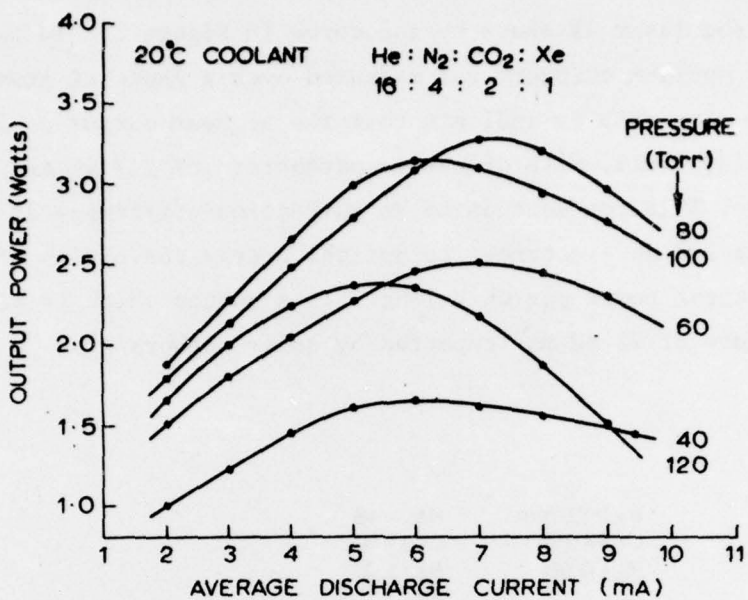romachined copper mirror which had been thorium fluoride coated, mounted at the centre of the bimorph bender, and a zinc selenide output mirror with a nominal 95 per cent reflectivity. In earlier experiments we obtained very good results from the use of freshly micromachined copper surface mirrors but have observed in this state two disadvantages. First, following seal-off, the reflectivity is at its highest, but in a matter of hours, surface oxidation and the resulting tarnishing effect causes a significant reduction in reflectivity. Second, a further deleterious effect caused by the oxidation process, is the removal of oxygen from the discharge gases. This causes the CO_2 dissociation equilibrium to be set far to the right and consequently seriously reduces the sealed lifetime of the laser. A thin coating of thorium fluoride appears to prevent the onset of these two effects while not materially affecting the reflectivity. The zinc selenide mirror used in these experiments had a measured 2.5 per cent absorption loss due largely to the

1.7

use of far more than the usual number of dielectric layers, in an attempt to produce a highly dispersive mirror. When operated with standard 'wide-band' coatings on a gallium arsenide mirror of the same nominal reflectivity, substantially more power was extracted from the laser as shown by the curve in Figure 6. In this experiment the power output at optimum current was measured over a range of pressures between 5.3 kPa and 19 kPa. The results indicate that the highest output of 3.85 W was obtained at 12 kPa (90 Torr), with discharge parameters of 2.7 kV and 8 mA in each leg of the discharge. This corresponds to an extraction efficiency of some 41 mW mm^{-1} of plasma and an electrical to optical energy conversion efficiency of 9 per cent. This output power per unit length is a number which is significantly larger than the figure of 22 mW mm^{-1} reported by other authors[1,8].
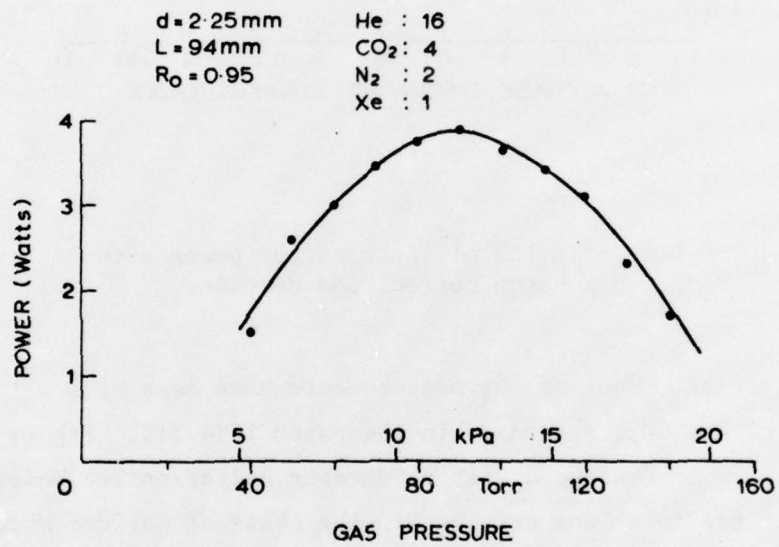
FIGURE 6. Variation of laser output power at optimum discharge current with pressure.

If we assume that all dissipative cavity losses are completely negligible so that the only loss of circulating power is by output coupling, then the maximum power per unit length extractable from a laser medium is obtained from Rigrod's power equations[9] as

$$\left[\frac{P}{L}\right]_{max} = I_s A g_o \qquad (1)$$

where I_s is the saturation intensity, g_o is the small signal gain, and A is the affective mode area. We have not as yet made direct measurements of either gain or

1.8

saturation intensity but an estimate of the maximum power available per unit length for our laser can be obtained from values of I_s and g_o reported in the literature. Klein and Abrams[10], have measured saturation intensity as a function of pressure and current for a gas mixture similar to ours. By extrapolation of their data at 12 kPa to our operating current of 8 mA we obtain a value of $I_s = 57.5$ W mm^{-2} This is in good agreement with the data obtained by Degnan et al[3] who quote a rise in saturation intensity of approximately 375 mW mm^{-2} Pa^{-1} (50 W cm^{-2} Torr^{-1}) when operating at a current of 8 mA. The question of gain is somewhat more of a problem, in that direct gain measurements are not available for the 2.25 mm bore tube which we used. However, if we assume that the similar discharge scaling laws are applicable over this range we can use the results of Abrams and Bridges[1] for a 1.5 mm bore amplifier. In this fashion we arrive at a value of g_o of 0.01 cm^{-1} as the most optimistic estimate for a 4:1 mixture where we are assuming the 'best' situation where the gain actually peaks at our operating pressure. If we write $A = \pi\omega^2$, where ω is the e^{-1} intensity radius of the Gaussian beam which matches best the EH$_{11}$ waveguide mode, and is given[11] by $\omega = 0.46a$ where a is the guide radius, we obtain on substitution of the values of I_s, g_o and A in equation (1) a value for maximum P/L of about 46 mW per mm. This value is consistent with our experimental power measurements.

4. CONCLUSION

We have designed, constructed and operated a cw CO_2 waveguide laser which is capable of producing a specific output power (watts per mm of gain medium) which is almost a factor of two larger than previously reported and which is consistent with the power extraction per unit length calculated on the basis of zero cavity dissipative losses.

REFERENCES

1. ABRAMS, R.L. and BRIDGES, W.L., *IEEE J. Quantum Electronics*, Vol. QE-9, No. 9, Sept. 1973, pp 940-946.

2. BRIDGES, T.J., BURKHARDT, E.G. and SMITH, P.W., *Opt. Commun.*, Vol. 6, Oct. 1972, pp 193-195.

3. DEGNAN, J.J., WALKER, H.E., McELROY, J.H. and McAVOY, N., *IEEE J. Quantum Electronics*, Vol. QE-9, April 1973, pp 489-491.

4. ABRAMS, R.L., *Appl. Phys. Lett.*, Vol. 25, No. 5, Sept. 1974, pp 304-306.

5. MARCATILI, E.A.J. and SCHMELTZER, R.A., *Bell Syst. Tech. J.*, Vol. 43, July 1964, pp 1783-1809.

6. HALL, D.R., GORTON, E.K. and JENKINS, R.M., to be published in *Journal of Applied Physics*.

7. McELROY, J.H., THOMPSON, P.E., WALKER, H.E., JOHNSON, E.H., RADECKI, D.J., REYNOLDS, R.S., *Appl. Optics*, Vol. 14, June 1975, pp 1297-1302.

8. MOCKER, H. and KOEHLER, T., paper given at the *Electro-Optics International 75 Conference*, Nov. 1975, Anaheim, California.

9. RIGROD, W.W., *J. Appl. Phys.*, Vol. 36, 1965, pp 2487-2490.

10. KLEIN, M.B. and ABRAMS, R.L., *IEEE J. Quantum Electronics*, Vol. QE-11, No. 8, August 1975, pp 609-615.

11. ABRAMS, R.L., *IEEE J. Quantum Electronics*, Vol. 21, Dec. 1972, pp 576-578.

10-MICRON PROPAGATION LOSSES IN HOLLOW DIELECTRIC WAVEGUIDES

D. R. Hall, E. K. Gorton and R. M. Jenkins

ABSTRACT

Measurements have been made of the propagation losses of $10\mu m$ radiation in hollow dielectric tubes of the type commonly used in the fabrication of waveguide CO_2 lasers. The dependence of such losses on the waveguide diameter and material were investigated and are compared with values calculated from theory. The attenuation coefficient of the fundamental hybrid EH_{11} mode is seen to vary inversely as the diameter cubed and to be very sensitive to tube camber and to the presence of impurities adhering to the wall surface.

10 MICRON PROPAGATION LOSSES IN HOLLOW DIELECTRIC WAVEGUIDES

D. R. Hall, E. K. Gorton and R. M. Jenkins

INTRODUCTION

There has been considerable activity in recent years in the development of cw carbon dioxide lasers at gas pressures in the range 6.7×10^3 to 46.7×10^3 Pa (50-350 Torr)[1-4]. Much of this work stems from the desire to increase the range of continuous frequency tunability which is possible in this pressure region, where molecular collisions provide the dominant broadening mechanisms. Wideband 10-micron sources of this type have potential applications in both optical radar and communications[5] besides providing a powerful spectroscopic tool. Experience has shown that the stable operation of continuous discharges in suitable CO_2-containing gas mixtures at these pressures can only be achieved under conditions where the plasma is confined in a small bore dielectric tube. For the pressure range of interest the bore sizes are in the range 0.75-3.0 mm. The use of 'conventional' laser resonators and free-space Gaussian mode propagation with discharge tubes of this size results in diffraction losses which are so high as to preclude laser oscillation. This has led to the application of the waveguiding techniques first proposed by Marcatili and Schmeltzer[6]. Tolerably low losses may only be achieved in these circumstances if the electromagnetic field propagates in a mode of the dielectric waveguide tube (which also serves to confine the discharge) and if the resonator is appropriately designed to minimise coupling losses[7-10]. As a consequence, the design of efficient waveguide lasers requires data on the propagation losses in the modes of interest. In addition one needs to know the dependence of such losses on the internal diameter of the tube and on the material from which it is constructed.

In this paper we present the results of a series of experiments of propagation losses sustained by 10-micron radiation when coupled into hollow dielectric waveguides. Measurements have been performed on the dependence of these losses on tube bore for a range of materials which are commonly considered for the construction of waveguide lasers.

THEORY

The electric field configurations and propagation constants of low order modes of the straight dielectric waveguide have been comprehensively treated by Marcatili and Schmeltzer[6]. For convenience, and in order to facilitate comparison

with the experiments, the relevant results from their work are reproduced and briefly discussed here.

There are three fundamental types of mode which are supported by a hollow dielectric tube of the type we are considering; first, transverse circular electric modes which have their electric field tangential to the guide surface; second, transverse circular magnetic modes whose magnetic field is tangential to the guide; and finally, hybrid modes which have both radial and tangential electric field components. If one makes the physically appropriate assumption that the wavelength of the optical field is very much smaller than the guide radius, a, the expressions for the electric field distribution are considerably simplified. In fact, Marcatili and Schmeltzer embody this assumption in the approximation

$$ka = \frac{2\pi a}{\lambda} >> |\nu| u_{nm} \tag{1}$$

where ν is the refractive index of the wall material, u_{nm} is the mth root of the equation $J_{n-1}(u_{nm}) = 0$, n and m are integers which characterize the propagating waveguide mode.

Of these three classes of modes, we are only concerned in this paper with the hybrid group, because of the conditions of our experiment and because of the importance of the lower order hybrid modes, which are in general much less lossy in waveguide laser technology. The radial and angular components of the electric field of the hybrid EH_{nm} class of modes may be written as

$$E_{rnm} = J_{n-1}(u_{nm}r/a)\sin n\Theta \exp[i(\gamma z - \omega t)]$$

$$E_{\Theta nm} = J_{n-1}(u_{nm}r/a)\cos n\Theta \exp[i(\gamma z - \omega t)] \tag{2}$$

where it is assumed that propagation is in the z direction and γ is the complex propagation constant given by

$$\gamma \simeq k\left[1 - \tfrac{1}{2}\left(\frac{u_{nm}\lambda}{2\pi a}\right)^2 \left(1 - \frac{i\nu_n\lambda}{\pi a}\right)\right] \tag{3}$$

where ν_n is a function of the waveguide wall material and also depends on the class of waveguide mode. For EH_{nm}, ν_n may be written as

$$\nu_n = \frac{\nu^2 + 1}{2(\nu^2 - 1)^{1/2}} \tag{4}$$

Taking the real and imaginary parts of γ we obtain the phase constant β_{nm}, and the attenuation coefficient α_{nm} as follows:

$$\beta_{nm} = k \left[1 - \frac{1}{2}\left(\frac{u_{nm}\lambda}{2\pi a}\right)^2 \left[1 + Im\left(\frac{\nu_n \lambda}{\pi a}\right)\right]\right] \tag{5}$$

$$\alpha_{nm} = \left(\frac{u_{nm}}{2\pi}\right)^2 \frac{\lambda^2}{a^3} Re\left\{\frac{\nu^2 + 1}{2(\nu^2-1)^{1/2}}\right\} \tag{6}$$

Equation (6) describes the dependence of the waveguide propagation loss for hybrid modes on the order of mode, the wavelength, and the bore and refractive index of the tube. This represents the most important result from the standpoint of the experiments to be described in this paper. Abrams and Bridges[2] have calculated $Re(\nu_n)$ as a function of wavenumber for the materials of most interest for waveguide laser applications, deriving their refractive index data from single crystal measurements made in various crystal orientations. However, in practice poly-crystalline, compressed forms of both alumina and of beryllia are used in laser fabrication. As an approximation to the real situation we have used in our calculations a value of $Re(\nu_n)$ averaged over the different crystal orientations.

In the experiment to be described later the objective was to excite the fundamental hybrid mode in a dielectric waveguide and measure the attenuation as the optical signal propagated in the guide. To ensure that the relevant mode was excited, the intensity distribution at the limit of the guide was monitored. The expected field distribution at some distance away from the guide, assuming that a perfect EH_{11} mode is propagating in the guide, may be obtained using the diffraction theory and applying the Fresnel approximation. The intensity distribution in a plane at a distance l from the guide is given[11] by

$$I(r,\theta,l) = |E(r,\theta,l)|^2 = \left(\frac{ka^2}{2l}\right)^2 \left[C^2 + S^2\right] \tag{7}$$

where

$$C = \int_0^1 dw \, \cos\left(\frac{ka^2 w}{2l}\right) J_o(u_{11}\sqrt{w}) J_o\left(\frac{kar}{l}\sqrt{w}\right)$$

$$S = \int_0^1 dw \, \sin\left(\frac{ka^2 w}{2l}\right) J_o(u_{11}\sqrt{w}) J_o\left(\frac{kar}{l}\sqrt{w}\right) \tag{8}$$

These expressions were evaluated for a distance $l = 40$ cm, equal to that used

experimentally, and are plotted as the solid curve in Figure 5. The integrations were performed in a trapezoidal approximation and converged after some twenty terms.

EXPERIMENT

The basic experimental arrangement is shown in Figure 1. The linearly polarised output from a stable, conventional carbon dioxide laser, oscillating on the P(20) line of the 001-100 transition in a fundamental TEM_{00q} mode and attenuated to about 1.5 W using a pair of rotatable germanium plates is incident on
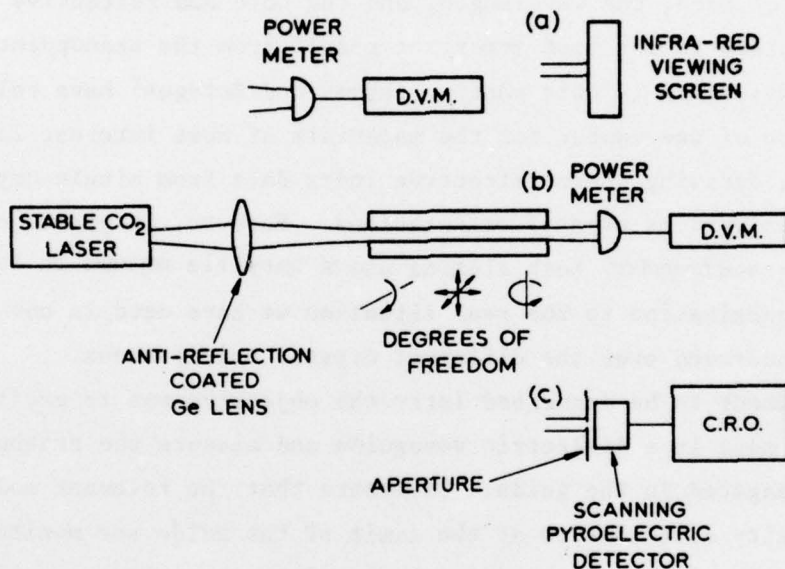
FIGURE I. Basic experimental arrangement

an anti-reflection-coated germanium lens. The lens of focal length f_L is used to focus the incoming signal to a spot size, $2\omega_o$, at the entrance to the waveguide whose transmission it is desired to measure. The task here is to couple a fundamental mode Gaussian beam into the waveguide in such a manner as to excite most efficiently the fundamental hybrid waveguide mode, EH_{11}. This problem has been addressed by Abrams[7] who used the technique of expanding the fundamental waveguide field amplitude distribution as a complete set of free space Gaussian normal modes in such a way as to maximise the coefficient of the lowest order mode. It is found that the value of ω_o/a which maximises this coefficient, and hence

which produces an optimum coupling situation, is 0.6435. Under this condition, 98% of the fundamental Gaussian signal at the input is coupled to the desired EH_{11} mode, while in excess of 99% is coupled into the guide overall. We therefore chose our lens focal length to satisfy the condition[12]

$$f_L = \frac{0.6435 \pi a D}{2\lambda} \qquad (9)$$

where D is the beam diameter at the $1/e^2$ intensity points incident on the lens. The coupling efficiency is therefore clearly very dependent on the exact separation d between the lens and the guide. This is illustrated by the curves in Figure 2 which show the dependence of the percentage transmission of the fundamental mode as a function of d/f_L. On the graph the calculated variation of spot size (2ω)
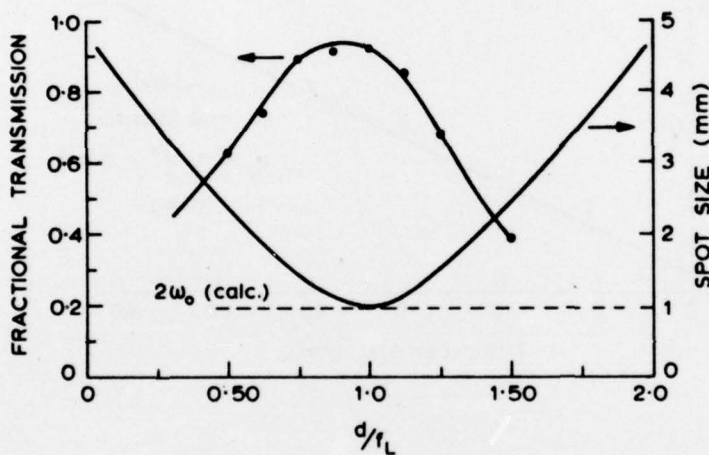
FIGURE 2.   Dependence of transmitted spot size on
             lens-to-waveguide separation for a 1.5 mm
             bore alumina tube

at the guide entrance is plotted and the calculated 'optimum' spot size $2\omega_o$ indicated. Optimum coupling is obtained near $d/f_L = 1$ where the condition of equation (9) is most closely satisfied.

Even under favourable coupling conditions there is still a finite and unknown coupling loss, the exact magnitude of which is not known, and which must be taken into account if accurate measurements of the propagation loss constant are to be made. If we write the total fractional transmission T through a waveguide tube of length L as

$$T = e^{-(\delta + aL)} \qquad (10)$$
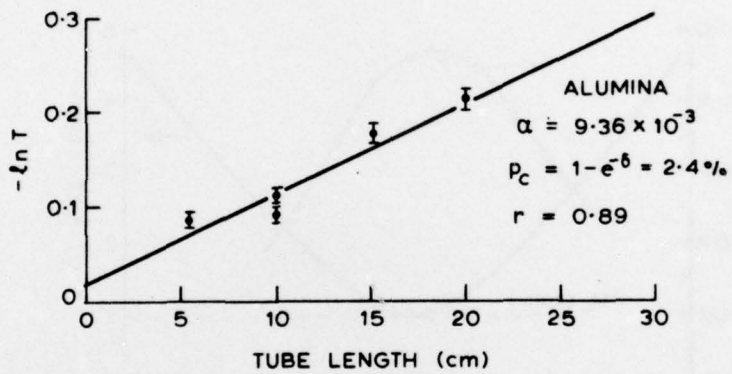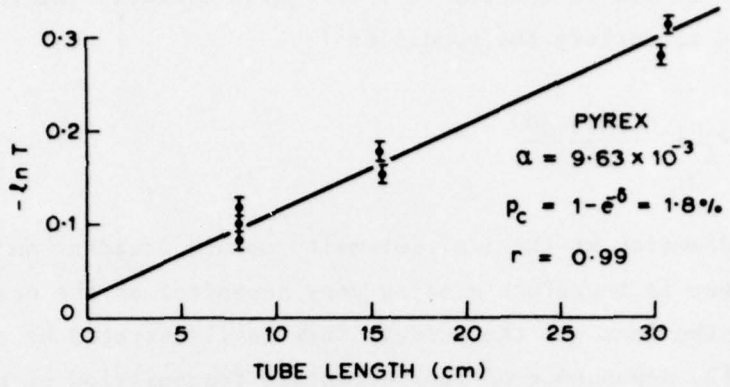
FIGURE 3.   Variation of power transmission
with length for 0.75 mm bore Pyrex
and alumina tubes.
(r = correlation coefficient).

δ is related to the coupling loss p_c by the equation

$$p_c = 1 - e^{-\delta} \tag{11}$$

In order to separate coupling from propagation losses, an experiment was designed so
that a series of transmission measurements were made on a waveguide whose whole
length was progressively shortened by carefully breaking lengths off. The complete
waveguide was mounted in such a way as to provide three translational and two
rotational degrees of freedom. Careful adjustments were made to provide optimum

2.8

transmission and then a check was made of the mode pattern either with a thermal infra-red screen or by scanning a detector across the beam to ensure that no higher order modes had been excited. Then the waveguide was shortened and the procedure repeated. In this manner data were obtained for Pyrex and alumina tubes of 0.75 mm bore from which a plot of $-lnT$ versus waveguide length could be drawn as shown in Figure 3. From the graphs we can obtain both the coupling loss in each case and also the propagation loss coefficient α from the calculated best fit straight line.

A series of such transmission experiments was performed on selected Pyrex and alumina tubes with bores from 0.75 to 2.5 mm which is the range of most interest for waveguide CO_2 laser fabrication.
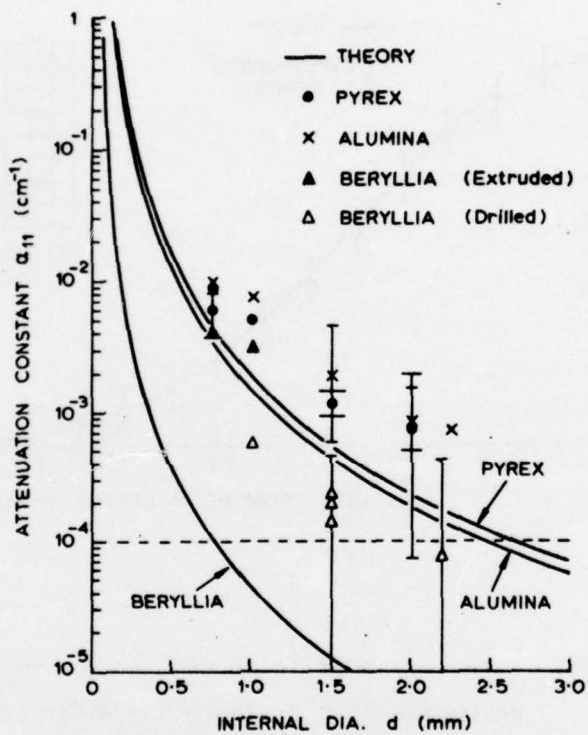
FIGURE 4.   Variation of attenuation constant α_{11} with internal diameter of waveguide for Pyrex, alumina and beryllia tubes

The results of these experiments are shown in Figure 4. The solid curves are plots of the theoretically predicted variation of propagation loss with diameter from equation (6) with the constants used as described above, while each point is the result of a slope determination from a plot similar to those in Figure 3.

In order to check that the mode of the guide which has been excited was in fact the EH_{11} mode, measurements were made of the beam profile at a distance l from the exit of the guide. A pyroelectric detector was scanned across the beam

and a plot obtained of the variation of intensity with radial distance. These points are plotted in the graph in Figure 5. The solid line is the theoretical curve obtained from a calculation of the transverse intensity distribution in the plane a distance 400mm from the end of the guide, with the assumption that a perfect EH_{11} mode as described by equation (7), is launched from its end. The very good fit is interpreted as assurance that it is in fact transmission of the fundamental hybrid mode whose propagation has been measured. The attainment of single mode patterns
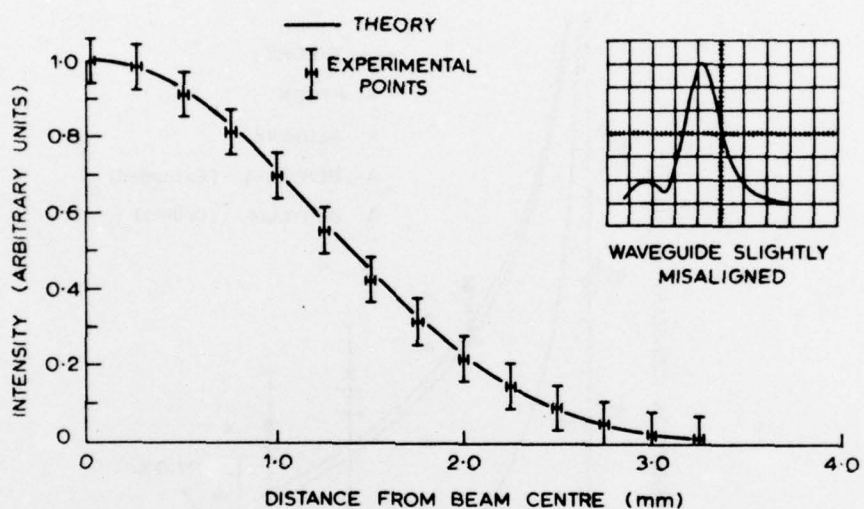
FIGURE 5.   Intensity profile of EH_{11} mode from a 2 mm bore
waveguide at a distance l = 400mm

such as that shown in Figure 5 requires very careful alignment of the waveguide. Even a slight misalignment will result in the excitation of combinations of modes, as is illustrated by the scan pattern shown in the inset which was obtained following a deliberate tube misalignment of a few milliradians.

DISCUSSION

In general, our experimental results for the variation of attenuation coefficient with waveguide diameter in Pyrex and alumina tubes are in good agreement with theory in that they exhibit the predicted a^{-3} dependence. However, the Pyrex and alumina losses are larger than the calculated values by about a factor

2.10

of three. While recognizing that the precise relevance of the calculated curves depends on the accuracy of the values of $Re(\nu_n)$ which are estimated for the polycrystalline material from single crystal measurements, we suggest that the loss discrepancy may be explained in terms of two additional sources of propagation loss over and above that described by equation (6). The first is the result of any departure from straightness of the waveguide bore. This question has been discussed by Marcatili and Schmeltzer[6] who have treated the case of a uniform bend of curvature R. They have shown that in such a case there is in addition to α_{11} a further loss term α_R given for the EH_{11} mode by the expression

$$\alpha_R = \left(\frac{2\pi}{u_{11}}\right)^2 \frac{a^3}{(\lambda R)^2} ReV_{11}(\nu) \tag{12}$$

where $ReV_{11}(\nu)$ is a function of the complex refractive index and the angle between the plane of the guide curvature and the direction of polarisation of the propagating radiation. Substitution of the appropriate value into equation (12) indicates that the difference between observed loss and calculated *straight* guide loss may be explained in terms of a uniform bend in the waveguide of 75 metres radius of curvature. In a tube 300mm in length this corresponds to a tube camber of about 1 part in 10^3, which is certainly less than the camber expected for the tubes used. The Pyrex and alumina waveguides were selected by visual inspection for straightness but a camber of 1 part in 10^3 is rather difficult to detect in tubes of the length used. It also represents a degree of straightness which is close to the limit of that attainable in drilled holes[13]. The second possible source of additional transmission loss is scattering due to either lack of inner wall smoothness or to minute contaminant particles on the inside of the tube. In selected cases we have polished the inner wall of alumina and Pyrex tubes using diamond paste and a suitable mandrel. In general, we have found that while polishing extruded tubes does improve transmission somewhat, the transmission loss was far more sensitive to any slight traces of foreign matter on the inner walls, so that rigourous cleaning is essential for tubes destined for use as lasers.

In interpreting the observed data for beryllia tubes, it must be realised that one is faced with the problem that the accuracy with which one can determine the difference between entrance and exit intensity effectively restricts measurements to tubes with overall losses above a certain limit. In practice, because of the extreme difficulty in maintaining straightness over long tube lengths, the limited tube lengths available set a lower limit to the measurable attenuation coefficient. We estimate that the stability of the laser and the accuracy of our power measurements put this lower limit at about 10^{-5}mm^{-1}, as indicated by the dashed line in Figure 4.

In contrast to the methods used to determine α [11] for alumina and Pyrex, the data plotted for beryllia are the result of a single transmission measurement on a given tube. This procedure was followed because of our reluctance to cut off pieces of beryllia owing to the health hazard associated with powdered beryllium oxide. We used values of coupling loss which had been obtained from measurements on Pyrex and alumina tubes of the same bore.

From the practical standpoint of assembling waveguide CO_2 lasers, we have adopted the practice in our laboratory of making transmission measurements on every tube before assembly. We measure transmission before and after electrode holes (usually four) are drilled radially into the guide, and also after assembly before the optics are added. We have found that guiding losses of less than 1% can be achieved and measured and that 1 mm diameter electrode holes make a negligible difference to transmission. With a 2.25 mm bore beryllia waveguide we have achieved 3.85 watts power output from a discharge 95 mm long[14].

CONCLUSIONS

A series of experiments has been performed to measure the optical transmission loss of hollow dielectric tubes typical of those used in the fabrication of waveguide carbon dioxide lasers. Comparison of experimental results with theoretical calculations confirms the expected a^{-3} dependence but indicates that the measured losses are somewhat larger than predicted. The discrepancy is explained in terms of additional losses introduced by the guide curvature. Lasers fabricated from tubes with measured guiding losses of less than 1% have been demonstrated to operate with high output powers per unit discharge length ($\sim$400 mW/cm) indicating very low overall losses[14].

REFERENCES

1. BRIDGES, T.J., BURKHARDT, E.G. and SMITH, P.W., *Opt. Commun.*, Vol. 6, 1972, pp 193-195.

2. ABRAMS, R.L. and BRIDGES, W.B., *IEEE J. Quantum Electronics*, Vol. QE-9, No. 9, 1973, pp 940-946.

3. DEGNAN, J.J., *J. Appl. Phys.*, Vol. 45, No. 1, 1974, pp 257-262.

4. ABRAMS, R.L., *Appl. Phys. Lett.*, Vol. 25, No. 5, 1974, pp 304-306.

5. McELROY, J.H., McAVOY, N., JOHNSON, E.H., GOODWIN, F.E., PEYTON, B.J., *NASA X Document* X-723-75-171. 1975 (To appear in Proc. IEEE).

6. MARCATILI, E.A.J., and SCHMELTZER, R.A., *Bell Syst. Tech. J.*, Vol. 43, 1964, pp 1783-1809.

7. ABRAMS, R.L., *IEEE J. Quantum Electronics*, Vol. QE-8, 1972, pp 838-842.

8. DEGNAN, J.J., and HALL, D.R., *IEEE J. Quantum Electronics*, Vol. QE-9, No. 9, 1973, pp 901-910.

9. CHESTER, A.N. and ABRAMS, R.L., *Appl. Phys. Lett.*, Vol. 21, 1972, pp 576-578.

10. ABRAMS, R.L. and CHESTER, A.N., *Appl. Optics*, Vol. 13, No. 9, 1974, pp 2117-2125.

11. DEGNAN, J.J., *Appl. Optics*, Vol. 12, 1973, pp 1026-1030.

12. KOGELNIK, H. and LI, T., *Appl. Optics*, Vol. 5, 1966, pp 1550-1566.

13. MOCKER, H., (*personal communication*).

14. HALL, D.R., JENKINS, R.M., GORTON, E.K. and CROSS, P.H., (*this volume*).

CARRIER RECOMBINATION AT DISLOCATIONS IN

GALLIUM PHOSPHIDE EPITAXIAL LAYERS

J. M. Titchmarsh*, G. R. Booker*,

W. Harding and D. R. Wight

ABSTRACT

The nature of dark spots observed in cathodoluminescence micrographs of gallium phosphide epitaxial layers has been examined using the transmission electron microscope and etching studies. Each dark spot is shown to be located at the intersection of a dislocation with the layer surface. Moreover screw, edge and mixed dislocations all give rise to spots of similar size and intensity. It is suggested that enhanced non-radiative recombination which gives rise to the dark spots is due to the core structure, rather than a concentration of dopant atoms, method of layer growth etc. and that different core structures are equally effective.

* Department of Metallurgy and Science of Materials,
  University of Oxford, Oxford.

CARRIER RECOMBINATION AT DISLOCATIONS IN

GALLIUM PHOSPHIDE EPITAXIAL LAYERS

J. M. Titchmarsh, G. R. Booker,

W. Harding and D. R. Wight

1. INTRODUCTION

There is interest at present in increasing the efficiency of GaP green light-emitting diodes (LED's). Such diodes are generally made using either vapour phase epitaxy (VPE) or liquid phase epitaxy (LPE) GaP layers grown on pulled single-crystal GaP substrates, the layers containing suitable dopants and nitrogen. The nitrogen provides efficient isoelectronic radiative recombination centres which have to compete with the non-radiative recombination centres present in the material. Recent work has shown that poor diode efficiencies are often associated with high densities of grown-in dislocations[1,2].

For good diode efficiencies, the epitaxial layers should possess good luminescence properties before the diodes are fabricated, as indicated by either high bulk photoluminescence (PL) efficiency[3] or high bulk cathodoluminescence (CL) efficiency[4]. Both of these luminescence efficiencies η are proportional to the minority carrier lifetime τ for the particular material[3,5]. The lifetime τ in turn depends on the density ρ of grown-in dislocations when ρ is sufficiently large[6,7,8]. This occurs because as ρ increases, the mean distance d between dis-locations decreases, and when d becomes comparable with the minority carrier diffusion length L for the corresponding low dislocation density material, the dislocations then control both L and τ, i.e. the dislocations become the dominant non-radiative recombination centre. Consequently, as ρ increases, τ decreases, and this causes η to decrease, and hence also the diode efficiency. In one investi-gation τ was also shown to be proportional to the concentration of a trap located 0.75 eV above the valence band[5], and it is tempting to associate this trap with the grown-in dislocations. Work on materials other than GaP has also shown that τ decreases as ρ increases e.g. on Ge[9,10], Si[10,11] and GaAs[12].

Direct evidence for non-radiative recombination occurring at individual dislocations in GaP has been obtained by recording micrographs using either electroluminescence (EL)[1], CL[2,13] or PL[16] signals to give the images. In such micrographs, the individual dislocations appear as dark spots. Similar micro-graphs were also obtained from GaP by using the electron beam induced conductivity signal[1]. For all of these microscopic techniques, the dark spots were correlated with grown-in dislocations either from the general appearance of the dark spot

3.3

distributions, or more rigorously by comparing the dark spots with etch pits in micrographs obtained from the same specimen areas. Work on materials other than GaP has revealed dark spots in micrographs using similar techniques, e.g. on Si[14], GaAs[15,16,17,18] and GaAs$_x$P$_{1-x}$[19].

Although the factors controlling the efficiencies of green LED's are now better understood, some points still need resolving if complete quantitative assessments are to be made. It is especially important to establish whether all types of dislocations, e.g. screw, 30°, 60°, edge, etc., are equally effective in acting as non-radiative recombination centres[2]. This is still uncertain because although there is a definite correlation between dark spots and etch pits, there is still doubt as to whether etching reveals all of the dislocations present[2]. Furthermore, etching does not enable one to distinguish between the different types of dislocation.

In order to obtain further information on this point, a combined CL, transmission electron microscope (TEM) and etch pit study has been made of several GaP epitaxial layer specimens. The main result of the investigation was that many different types of dislocation were present, and that all were extremely effective in acting as non-radiative recombination centres.

2. CATHODOLUMINESCENCE STUDIES

A range of epitaxial material was selected for investigation, including LPE layers grown in a horizontal furnace onto (111) or (100) oriented pulled-crystal substrates; sample dimensions were typically 2 to 4 mm. P-type layers were doped with Zn (N_A - N_D ∿5 x 10^{17} cm^{-3}), and n-type layers were undoped or doped with S, Te or Si (1 x 10^{14} cm^{-3} < N_D - N_A < 1 x 10^{18} cm^{-3}). Some samples had been nitrogen doped (concentration < 10^{18} cm^{-3}) by adding gaseous NH$_3$ to the hydrogen atmosphere in the furnace. A number of sulphur-doped, n-type, VPE layers* with and without nitrogen doping were also studied.

CL micrographs were obtained using a scanning electron microscope (Cambridge Stereoscan Mark IIA) with a specially developed CL mode detection system. A beam voltage of 30kV was employed with probe currents in the range 10^{-7} to 10^{-6}A and probe size 0.5μm diameter. The beam was incident normally on the sample's surface and the luminescence output was collected by a mirror system and detected with a photomultiplier tube (EMI 9658B S20 cathode), green luminescence being selected with an interference filter.

* Kindly supplied by Dr P Hart, Allen Clark Research Laboratories, Plessey Co., Ltd., Towcester, England.

A typical CL micrograph exhibiting dark spots is shown in Figure 1. All of the materials studied showed these features, although in a few instances some dark lines and/or more random shapes were present. In samples showing clearly defined, approximately circular spots, the densities of the features were in general variable across the surface of the epitaxial layer, although many samples showed a more or less uniform distribution. The dark spots were typically 5 to 7μm in diameter, and the density ranged from 5×10^3 to 10^6 cm^{-2}.
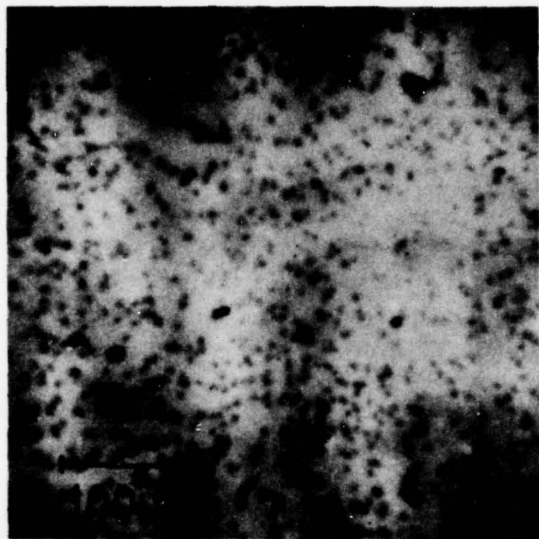

FIGURE I. A typical CL micrograph of a GaP epitaxial layer with a dark spot density of approximately 5×10^5 cm^{-2}.

Two samples with high luminescence efficiencies were selected for detailed study. (a) A (100) oriented, Si-doped, n-type (n = 1.0×10^{18} cm^{-3}), LPE sample with a layer thickness of 70μm, and (b) a (111)A oriented, Te-doped ($N_D - N_A = 1.3 \times 10^{18}$ cm^{-3}) LPE sample with a layer of thickness 95μm. The first sample was used to correlate the dark spots present in CL micrographs with dislocations observed using the TEM. The second sample was used to correlate the dark spots with etch pits.

3. TRANSMISSION ELECTRON MICROSCOPE STUDIES

To obtain an exact correlation of the dark spots with dislocations, it was necessary first to record CL micrographs of a specific area of the sample, and then to prepare a TEM specimen by thinning the sample in that same area, from the
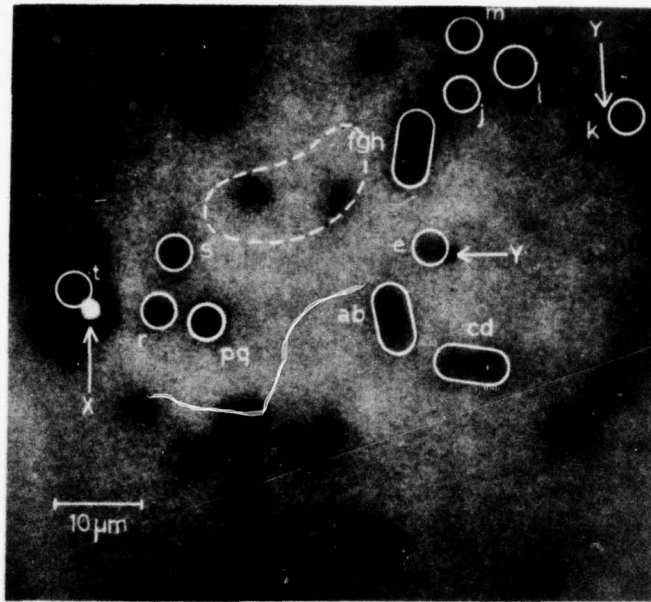
FIGURE 2.   A CL micrograph of a (100) oriented Si-doped GaP layer.
            The dashed line marks the position of a hole produced
            during the TEM specimen preparation of this same area.
            The feature marked X is a pinhole in the epitaxial layer
            and those marked Y are small particles of dirt. The
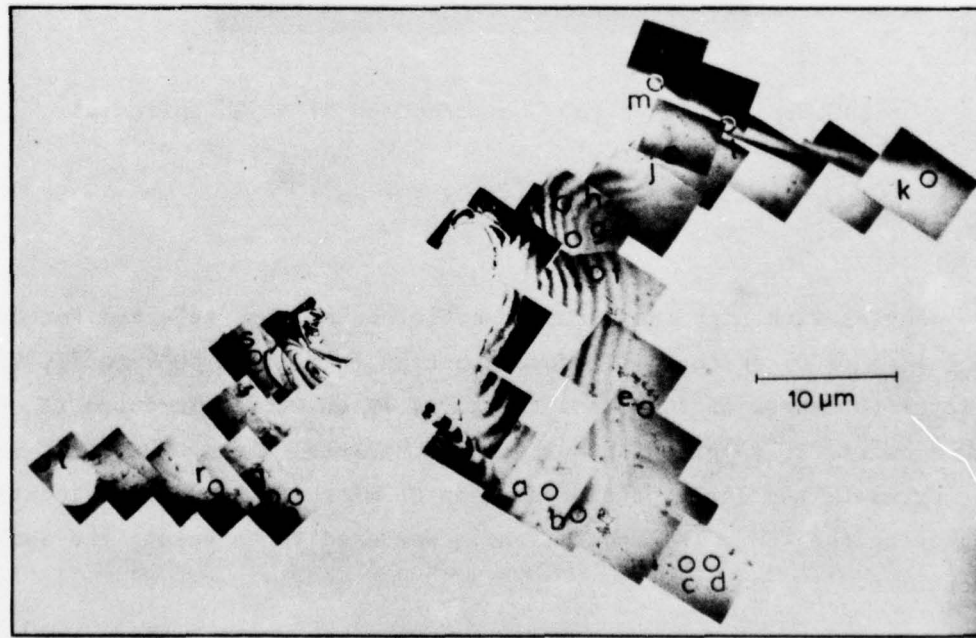   remaining letters refer to dark spots.

FIGURE 3.   A low-magnification TEM micrograph montage of part of
            the same area shown in Figure 2. The lettered circles
            mark the positions of dislocations in the thin foil and
            these can be compared with the positions of the
            lettered dark spots in Figure 2.

substrate side only, to a thickness of about 1 μm. Secondary electron emissive mode micrographs were recorded, corresponding to each CL micrograph, and the surface features in these micrographs registered with surface features observed in optical micrographs. The sample was then thinned by chemical jet polishing, using a solution of chlorine gas dissolved in methanol, until small holes appeared. More emissive mode and optical micrographs were recorded, and these enabled the positions of the holes to be drawn accurately on the CL micrographs.

Figure 2 shows a CL micrograph with the position of a subsequently formed hole indicated by the dashed line. The bright feature X corresponds to a pinhole in the epitaxial layer, and the dark feature Y to a small particle of dirt subsequently removed during the TEM specimen preparation. The area surrounding the hole and containing a number of dark spots was examined in an AEI EM7 electron microscope operating at 500kV.
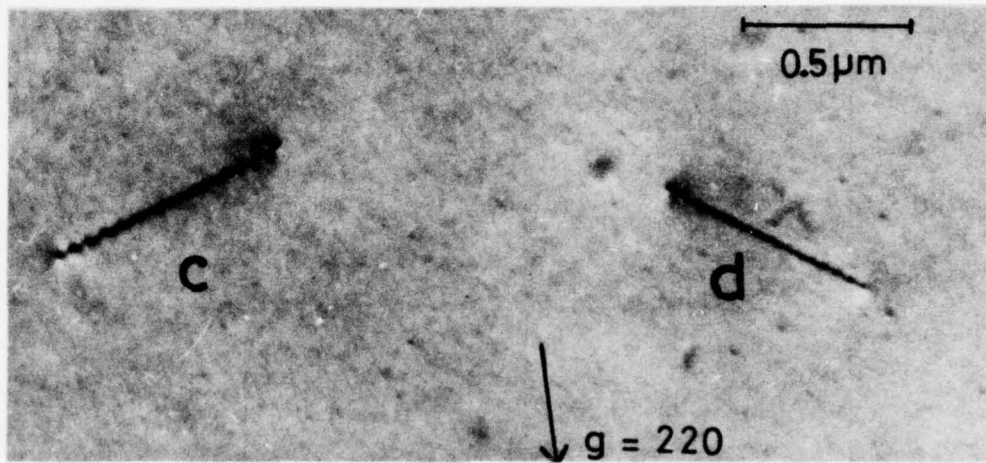

FIGURE 4. A higher magnification TEM micrograph of two dislocations which show typical oscillating contrast but no obvious precipitation.

The only structural features observed using the TEM were dislocations which threaded the foil. A low-magnification montage of transmission electron micrographs (Figure 3) was constructed so that the positions of a number of dislocations could be registered with respect to the position of the hole in the specimen and the pinhole X (Figure 2). Additional dislocations which had been out of contrast under the diffraction conditions used to record Figure 3, were observed when the foil was re-examined using different diffracting conditions. Some of the dislocations were seen better when the foil was tilted through large angles ($>30°$), these dislocations had been previously viewed end-on in Figure 3 and were less readily visible. Figure 4 shows two of the dislocations at a higher magnification.

Dislocation letter in Figure 3.	Burgers Vector[†]	Dislocation[†] Axis	Dislocation Type
a	$\frac{a}{2}[1\bar{1}0]$	$[001]$	90°
b	$\frac{a}{2}[01\bar{1}]$	$*[11\bar{2}]\rightarrow[0\bar{1}1]$	$0\rightarrow30^\circ$
c	$\frac{a}{2}[01\bar{1}]$	$*[1\bar{1}2]\rightarrow[0\bar{1}1]$	$0\rightarrow30^\circ$
d	$\frac{a}{2}[10\bar{1}]$	$*[\bar{1}12]\rightarrow[10\bar{1}]$	$0\rightarrow30^\circ$
e	$\frac{a}{2}[01\bar{1}]$	$[1\bar{1}2]$	30°
f	$\frac{a}{2}[01\bar{1}]$	$[01\bar{1}]$	0°
g	$\frac{a}{2}[110]$	$[001]$	90°
h	$\frac{a}{2}[10\bar{1}]$	$*[10\bar{1}]\rightarrow[\bar{1}12]$	$0\rightarrow30^\circ$
j	$\frac{a}{2}[01\bar{1}]$	$[01\bar{1}]$	0°
k	$\frac{a}{2}[01\bar{1}]$	$[01\bar{1}]$	0°
l	$\frac{a}{2}[110]$	$[001]$	90°
m	$\frac{a}{2}[110]$	$[001]$	90°
p	$\frac{a}{2}[101]$	$[001]$	45°
q	$\frac{a}{2}[10\bar{1}]$	$*[\bar{1}12]\rightarrow[10\bar{1}]$	$0\rightarrow30^\circ$
r	$\frac{a}{2}[110]$	$[0\bar{1}1]$	60°
s	$\frac{a}{2}[01\bar{1}]$	$*[011]\rightarrow[1\bar{1}2]$	$0\rightarrow30^\circ$
t	$\frac{a}{2}[101]$	$[101]$	0°

[†] A right-handed axis system is used with the foil normal [001]

* These dislocations do not lie exactly along low-index crystallographic directions, but between the two directions indicated and on the {111} slip planes containing these directions.

TABLE I

BURGERS VECTOR ANALYSES OF DISLOCATIONS

3.8

There was no evidence of precipitation on the dislocations, although an impurity atmosphere surrounding the dislocations could have been present without being detected by the TEM examination.

In every case it was found that a dislocation corresponded to a dark spot, and vice versa. A number of dark spots in Figure 2 have been circled and lettered for comparison with Figure 3. Each of the extended dark spots ab and cd in Figure 2 correspond to two dislocations about 3μm apart, whilst fgh in Figure 3 corresponds to three dislocations with similar separations. The spot lettered pq (Figure 2) is much darker than the others, and two dislocations less than 2μm apart were observed at that point.

Slight displacements of 1 or 2μm were sometimes observed between the two corresponding positions in the CL and TEM micrographs, and this can be at least partly explained in the following manner. Contrast in the CL mode depends upon the depth of penetration of the incident electron beam, which is several microns for the beam potential of 30 kV used in these experiments. Thus, the centre of the dark spots probably corresponds to the position of the dislocation typically 1 to 2μm below the epitaxial layer surface. For a dislocation inclined at 45° to the plane of the foil, this would give a displacement of 1 to 2μm relative to the point of termination of the dislocation in the specimen surface.

The nature of the seventeen dislocations lettered in Figure 3 were analysed in detail and the results are given in Table 1. All were perfect dislocations with $\frac{a}{2}$<110> Burgers vectors. Among the seventeen, five of the possible six different types of $\frac{a}{2}$<110> Burgers vectors were present (+$\underline{b}$ and -$\underline{b}$ were not distinguished). The crystallographic directions of the dislocations' lines were deduced from stereomicrographs and careful tilting experiments, and it was found that screw, edge and mixed dislocations were all present. Dislocations were observed at positions corresponding to the unlettered dark spots in Figure 2, but Burgers vectors were not determined for these dislocations.

4. ETCH PIT STUDIES

A CL micrograph (Figure 5a) of the (111) A oriented sample selected for this study showed a typical array of dark spots. The secondary electron emissive mode micrograph indicated that the specimen surface in this area was featureless.

The specimen was etched for 16 seconds in an aqueous solution of KOH (120g/litre) and $K_3Fe(CN)_6$ (80g/litre) heated to its boiling point, and the area shown in Figure 5a re-examined. The emissive mode micrograph (Figure 5b) showed clearly defined triangular etch pits which correlated with the positions of the dark spots in Figure 5a. A few less well defined, shallower etch features were present which do not correlate with dark spots. The triangular pits are typical

of dislocations, and the one-to-one correspondence between dark spots and dislocations obtained in Section 3 is thus confirmed by these etching studies. The two sets are in register to within 2μm, and the slight displacements (<2μm) can probably be caused either by the removal of material during etching or by the effect due to the penetration of the electron beam described above.
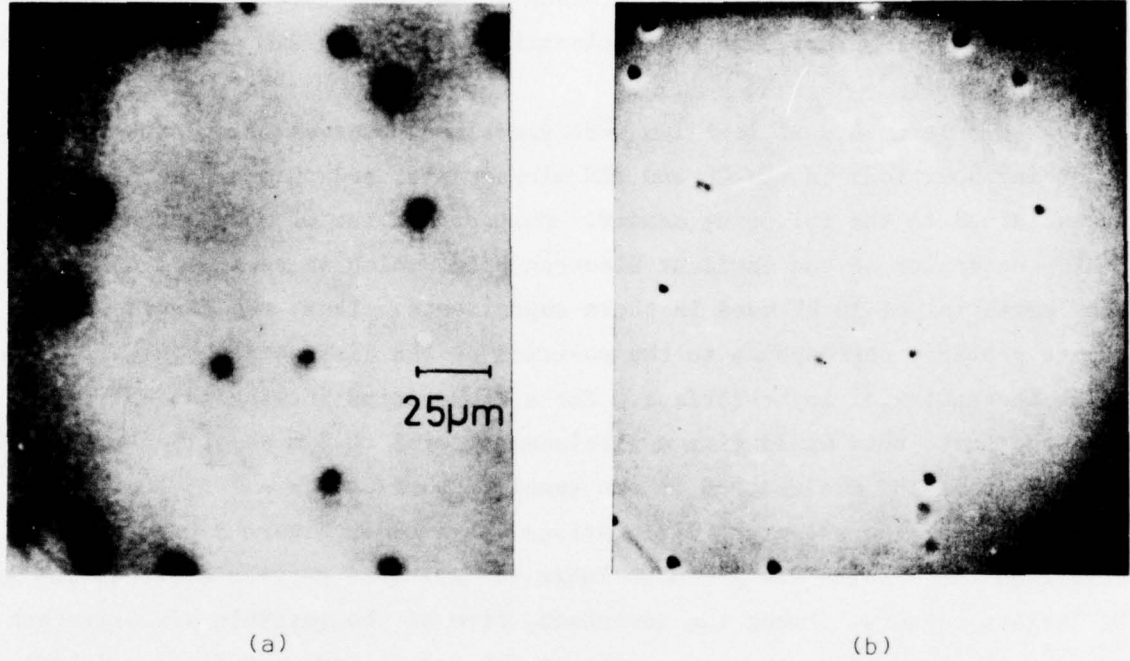

(a)   (b)

FIGURE 5.   (a)   A CL micrograph of the (III)A oriented Te-doped
                  layer and

            (b)   the same area after etching to reveal dislocation
                  sites imaged in the secondary electron mode of
                  an SEM

5. DISCUSSION

The combined CL and TEM examination of the same area of the GaP specimen has demonstrated conclusively there is a one-to-one correspondence between the CL dark spots and the dislocations emerging at the specimen surface. Each dark spot contained a dislocation, and each dislocation gave a dark spot. The only exceptions were when the dislocations were too close together (<5μm) for the dark spots to be resolved. The dark spots then either ran together to give elongated spots or became superimposed to give darker spots. A dark spot occurred regardless of the type of dislocation, i.e. whether screw, 30°, 60° or edge.

Two possible mechanisms may explain the effect of dislocations as non-radiative recombination centres. The recombination may be due either to some interaction between the dislocations and impurities or to point defects, or to a property of the dislocations themselves. The experimental results show that grown-in dislocations act as recombination centres in epitaxial material regardless of the method and temperature of growth, the type and concentration of dopant, or the crystallographic orientation. This suggests that neither impurity nor native defect (e.g. interstitial Ga or P atoms, or vacancies) interactions are the main reason for recombination behaviour. The results of Heinke and Queisser[18] in GaAs do not contradict this view, their investigation showing that interactions with impurities or point defects decrease the effectiveness of dislocations as non-radiative recombination centres.

If the effect is due mainly to the core or elastic strain field of the dislocations, then it might be expected to depend on the type of dislocation. The experimental results provide no evidence for this. A possible explanation may be that the different types of dislocations have different capture radii, different lifetimes in the captured state etc., but nevertheless all the types compete effectively with the recombination processes in the bulk of the crystal and hence appear similar in the present studies. The present work does not enable the dominant mechanism to be determined, but the overall results tend to suggest that it is an inherent property of the dislocation rather than a mechanism involving the interaction of impurities or point defects with the dislocation.

ACKNOWLEDGEMENTS

REFERENCES

1. STRINGFELLOW, G. B., LINDQUIST, P.F., CASS, T. R. and BURMEISTER, R. A., *J. Electron. Mater.*, Vol. 3, 1974, pp 497-515.

2. BRANTLEY, W. A., LORIMER, O. G., DAPKUS, P. D., HASZKO, S. E. and SAUL, R. H., *J. Appl. Phys.*, Vol. 46, 1975, pp 2629-2637.

3. DAPKUS, P. D., HACKETT, W. H., LORIMER, O. G., KAMMLOTT, G. W. and HASZKO, S. E., *Appl. Phys. Lett.*, Vol. 22, 1973, pp 227-229.

4. WIGHT, D. R., BIRBECK, J. C. H., TRUSSLER, J. W. A. and YOUNG, M. L., *J. Phys. D.*, Vol. 6, 1973, pp 1622-1639.

5. HAMILTON, B., PEAKER, A. R., BRAMWELL, S., HARDING, W. and WIGHT, D. R., *Appl. Phys. Lett.*, Vol. 26, No. 12, 1975, pp 702-704.

6. SUZUKI, T. and MATSUMOTO, Y., *Appl. Phys. Lett.*, Vol. 26, 1975, pp 431-433.

7. BLENKINSOP, I. D., HARDING, W. and WIGHT, D. R., *reported by P. J. Dean at International Conference on Luminescence*, Japan, September 1975, (in press).

8. KUIJPERS, F. P. G., BLOK, L. and VINK, A. T., *International Conference on Luminescence*, Japan, September 1975, (in press).

9. OKADA, J., *J. Phys. Soc., Japan*, Vol. 10, 1955, pp 1110-1111.

10. KURTZ, A. D., KULIN, S. A. and AVERBACH, B. L., *Phys. Rev.*, Vol. 101, 1956, pp 1285-1291.

11. HUNTER, D. R., PAXMAN, D. H., BURGESS, M. and BOOKER, G. R., *"Scanning Electron Microscopy: Systems and Applications 1973"*, Conference Series No. 18, (Institute of Physics, London and Bristol), p 208.

12. ETTENBERG, M., *J. Appl. Phys.*, Vol. 45, 1974, pp 901-906.

13. DAVIDSON, S. M., IQBAL, M. Z. and NORTHROP, D. C., *Phys. Stat. Solidi A*, Vol. 29, 1975, pp 571-578.

14. CZAJA, W. and PATEL, J. R., *J. Appl. Phys.*, Vol. 36, 1965, pp 1476-1482.

15. CASEY, H. C., *J. Electrochem. Soc.: Solid State Science*, Vol. 114, 1967, pp 153-158.

16. ZSCHAUER, K. H., *Solid State Commun.*, Vol. 7, 1969, pp 335-337.

17. ESQUIVEL, A. L., LIN, W. N. and WITTRY, D. B., *Appl. Phys. Lett.*, Vol. 22, 1973, pp 414-416.

18. HEINKE, W. and QUEISSER, H. J., *Phys. Rev. Lett.*, Vol. 33, 1974, pp 1082-1084.

19. KASANO, H. and HOSOKI, S., *J. Appl. Phys.*, Vol. 46, 1975, pp 394-401.

THE TRANSVERSE ENERGY OF ELECTRONS EMITTED FROM
GALLIUM ARSENIDE

D. J. Bradley, M. B. Allenson and B. R. Holeman

ABSTRACT

The mean transverse emission energy (MTEE) of electrons from GaAs photo-
cathodes has been derived from limiting resolution measurements on proximity
focused image intensifiers. The value of 107 ±18 meV obtained for the (111)B
emitting surface of $GaAs/Ga_xAl_{(1-x)}As/GaP$ photocathodes is approximately two
orders higher than that calculated by other workers, and does not depend on the
applied electric field in the range 1000-4000 V mm^{-1}. In contrast to previous
work a comparable value has also been measured at 2V mm^{-1} using a LEED optic
assembly with correction for the distortion of the trajectories of these very
low energy electrons. The rough emitting surface of practical photocathodes may
be responsible for the high transverse emission energies and a model is considered
in which electrons are emitted from a sinusoidal surface. It is shown that the
observed field independent MTEE is obtained with a period to amplitude ratio of
about four, and that the period lies between 2.5 and 100 nm. An initial study of
photocathode surfaces by scanning electron microscopy has shown that a surface
structure is produced by the heat-cleaning process on a scale which is within
this range.

THE TRANSVERSE ENERGY OF ELECTRONS EMITTED FROM
GALLIUM ARSENIDE

D. J. Bradley, M. B. Allenson and B. R. Holeman

1. INTRODUCTION

Negative Electron Affinity (NEA) photoemitters such as gallium arsenide, $Ga_x In_{1-x} As$ and silicon have potential as photocathodes in image intensifiers. They require semiconductor material with minority carrier diffusion lengths greater than about one micrometre and this can only be obtained in single crystal epitaxial layers of high perfection, which, with current growth technology, are necessarily flat. This largely precludes their use in inverter imager intensifiers, and limits their application to proximity focused diodes or triodes (if a channel plate is included).

The resolution of a proximity focused device is particularly sensitive to degradation by the component of the electron emission velocity parallel to the photocathode plane. However Burt[1], Pollard[2] and Bell[3] have all shown theoretically that mean transverse emission energies (MTEE) of 1-2 meV can be expected from NEA gallium arsenide. In addition Pollard[2] has reported MTEE of this order from gallium arsenide when using a LEED-Auger apparatus as an emission angle analyser, and Piaget et al[4] have measured 8 meV for $Ga_x In_{1-x} As$ in a proximity focused structure. These values are approximately two orders lower than those for multi-alkali photocathodes and suggest that NEA photocathodes may allow high resolution to be achieved at lower voltages and wider photocathode-to-phosphor gaps than are current in proximity focused image intensifiers incorporating multialkali photocathodes. Unfortunately, measured data on devices containing gallium arsenide photocathodes[5,6] fail to support these predictions and give values of about 100 meV.

In this paper the discrepancy is examined using the following approach. Firstly, in Section 2, the resolution as a function of applied voltage and of phosphor-to-photocathode gap is calculated. Secondly, in Section 3, the influence of a rough photocathode surface on the measured MTEE is examined. Two limiting cases can apply. The first, which we have termed the field distortion effect is that considered by Martinelli[7] and by James[8]. This can produce a high effective MTEE which is proportional to the applied field. The second, which we have called the slope effect, is the result of the initial velocity, near normal to the local surface, contributing to the mean velocity parallel to the overall photocathode plane. This can also produce a high MTEE which is now independent of the applied field.

The transverse energy measurements on proximity focused tubes are presented in Section 4. It is apparent that over the limited range of field strengths for

which measurements are practical, the MTEE is high, (about 100 meV) and also independent of applied electric field, suggesting that the field distortion effect does not apply. In Section 5 it is shown that severe errors can arise when using a LEED grid assembly for very low energy electrons. By correcting for these effects, an MTEE has been measured which is in agreement with that observed in proximity tubes, and which extends the range of field independence to as low as 2 V mm^{-1}. An examination of the photocathode surfaces by scanning electron microscopy is described in Section 6.
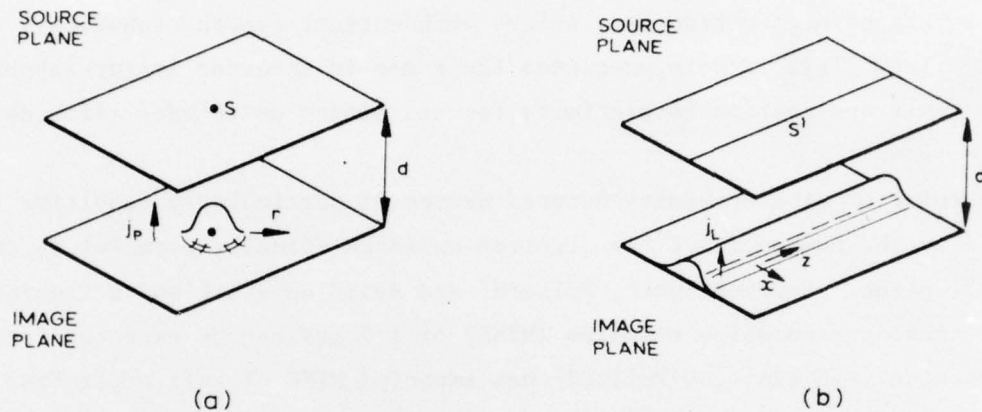

FIGURE 1. (a) Electron point spread function
(b) Electron line spread function.

2. THE MODULATION TRANSFER FUNCTION AND LIMITING RESOLUTION OF PROXIMITY FOCUSED TUBES

In a proximity focused image tube the lateral motion of the photo-electrons in the photocathode-to-phosphor gap will result in degradation of the image. This degradation is best described by the modulation transfer function (MTF) and this can readily be derived if the electron emission properties are known. The first step in this derivation is to compute the point spread function, i.e. the electron density distribution on the phosphor produced by a point source of electrons (S in Figure 1a). If an electron leaves the photocathode with a transverse velocity component v_T, it strikes the phosphor at a point distance r from the geometric image where, if τ is the transit time,

$$r = v_T \tau$$

4.4

If the electron transverse energy distribution is such that it can be described by a distribution function, N, with circular symmetry and with the form

$$n(v_T) = N(v_T/\bar{v}_T)dv_T$$

then the corresponding point spread function has the form

$$j_p = C_p P(R^2) .$$

Here $n(v_T)$ is the number of electrons with transverse velocity v_T and $\bar{v}_T$ the r.m.s. velocity. j_p is the current density at radius r from the geometric image, C_p is a normalising coefficient and R is a dimensionless radius given by $R = r/\bar{v}_T\tau$. This expression for j_p assumes that the initial velocity of the electron perpendicular to the photocathode is sufficiently small compared with the effect of the applied field, that the transit time can be taken as constant for all the electrons.

The equivalent line spread function of a line source S' shown in Figure 1b is then

$$j_L = \int_{-\infty}^{\infty} C_p P(X^2+Z^2)dZ = C_L L(X^2)$$

where j_L is the current density at distance x from the line, z is distance along the line, C_L is a normalising coefficient, X and Z are dimensionless and are given by $X = x/\bar{v}_T\tau$ and $Z = z/\bar{v}_T\tau$.

The MTF is given by the normalised Fourier transform of j_L, i.e.

$$\text{MTF} = C_M \int_{-\infty}^{+\infty} 2 \cos (2\pi FX) L(X^2)dX = M(F)$$

where C_M is a normalising coefficient, F is a dimensionless spatial frequency given by $F = f\bar{v}_T\tau$ and f is the spatial frequency.

The limiting resolution, f_L, of a device, given a suitable display and when not noise limited, varies over a limited range from observer to observer, but is now generally taken as the point where the MTF has fallen to 5%. Hence if F_L is given by $M(F_L) \doteq 0.05$ then

$$f_L = F_L/\bar{v}_T\tau.$$

Since $\tau^2 = 2dm/Ee$ where d is the cathode-to-anode gap, m and e are the electron mass and charge and E is the electric field, and $\bar{v}_T = 2(\bar{E}_T)^{\frac{1}{2}}/m$ where $\bar{E}_T$ is the mean energy of the emitted electrons parallel to the photocathode (MTEE) then $f_L = K(E/\bar{E}_T d)^{\frac{1}{2}}.$

The value of the constant K, is determined only by the form of the distribution

function and is insensitive to choice of this function. Needham[9] has shown that for a number of specific transverse velocity distributions, $K \simeq 8$ when f_L is in line pairs per mm, d is in mm, E is in kV mm^{-1} and $\bar{E}_T$ is in eV.

In particular it can readily be shown that if the transverse velocity distribution is Gaussian, i.e. N has the form

$$N = N_o \frac{v_T}{\bar{v}_T} \exp\left[-\left(\frac{v_T}{\bar{v}_T}\right)^2\right] dv_T$$

then $K = 8.7$ so that

$$f_L = 8.7\,(E/\bar{E}_T d)^{\frac{1}{2}} \tag{1}$$

Equation (1) can be applied in the case of a plane NEA photocathode surface since the transverse velocity distribution has been calculated[1,2] to have the form

$$n(v_T) = N_o\, v_T \exp\left[-\frac{m2}{m\star}\frac{v_T^2}{2kT}\right] dv_T$$

Here $m\star$ is the electron effective mass in the semiconductor, k is Boltzmann's constant and T is the absolute temperature. This expression is valid for small angles of emission ($\frac{1}{2}mv_T^2 \ll E_A$ where E_A is the NEA) and the corresponding angular distribution is

$$N(\theta) = N_o\, \theta \exp\left[\frac{-m}{m\star}\frac{E_A\theta^2}{kT}\right] d\theta \tag{2}$$

where θ is measured from the normal to the emitting surface. The MTEE is then given by

$$\bar{E}_T = \frac{m\star}{m}\, kT$$

For GaAs at room temperature, $\qquad \bar{E}_T \simeq 1.5$ meV.

3.   THE EFFECT OF SURFACE TOPOGRAPHY ON THE TRANSVERSE ENERGY

Practical III-V photocathode surfaces are unlikely to be completely plane. All the transmission photocathode structures using these materials are grown by epitaxy onto lattice matched or near lattice matched substrates, and this results in a characteristic topography[10,11] which may be modified by subsequent chemical etching.

Furthermore, the heat-cleaning, which is a necessary part of the activation procedure, may produce both facetting[12] and thermal etch pits[13]. This uneven surface has been considered as a possible cause of the effective high transverse energy by Martinelli[7] and by James[8]. They showed that surface structure on a

micrometre scale in combination with the high applied electric field in a
proximity tube results in a distorted field near the cathode in which the
electrons can gain transverse energy. We call this the field distortion effect.
A rough surface can also produce a field independent increase in transverse energy
which we term the slope effect. The electrons are emitted with a velocity component
parallel to the local surface, corresponding to an MTEE of 1-2 meV but with a local
normal velocity giving an energy of 100-200 meV. The components of these normal
velocities in the mean plane of the rough surface produce a contribution to the
MTEE which does not depend on the electric field.
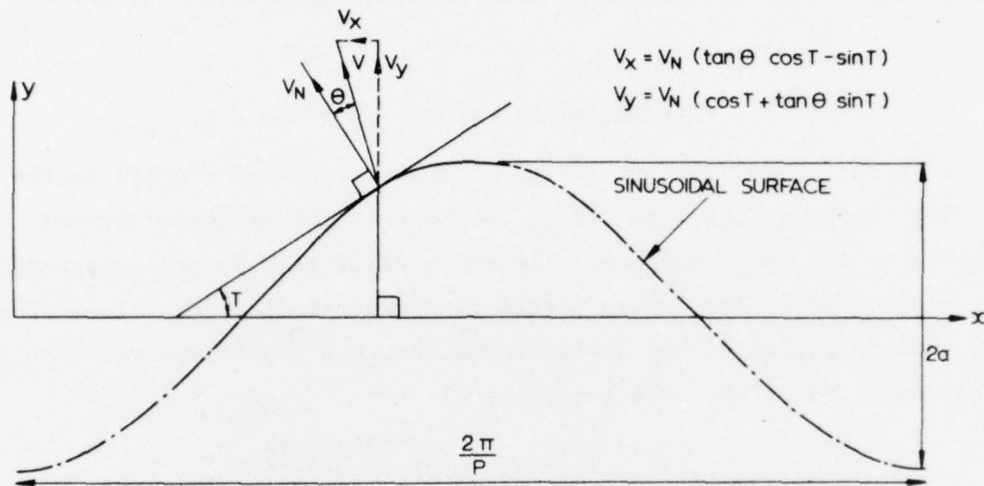
FIGURE 2. Velocity components of electrons emitted from a
sinusoidal photocathode surface

In this section the real photocathode surface is approximated by a surface
with sinusoidal corrugations and the mean transverse energy of the emitted
electrons is calculated. Both the field distortion effect and the slope effect are
taken into account and the dependance of the limiting resolution on the field and
spacing is obtained. The effect upon this dependance when one or other of the
effects dominates, is examined.

The potential distribution between a flat plate and a sinusoidal surface has
been derived by Klopfenstein and Wehner[14] who showed that for sufficiently small
deformations of the form $y = a \cos(px)$, only the first Fourier component need be
considered, in which case the potential is given by

$$V_{x,y} = E_o y - E_o a \exp(-py)\cos(px)$$

where E_o is the applied electric field when a is zero.

This leads to the following expression for the x and y components of the
electric field:

4.7

$$E_x = E_o ap \exp(-py) \sin(px)$$

$$E_y = E_o + E_o ap \exp(-py) \cos(px)$$

If the electron trajectory as a function of time is given by $x(t)$, $y(t)$ then the transverse velocity as a function of time for the surface shown in Figure 2 is given by

$$v_x(t) = v_N(\cos T \tan\theta - \sin T) + \frac{e}{m}\int_o^t E_o ap \sin[px(t)]\exp[-py(t)]dt \tag{3}$$

If the product ap is much less than unity, variations of the electric field in the y-direction can be neglected and if it is assumed that the x-displacement of the electron within the distorted field region is small compared with the period, then

$$x(t) = x_1$$
$$y(t) = v_N(\tan\theta\sin T + \cos T)t + eE_o t^2/2m \tag{4}$$

where x_1 is the point of emission of the electron, $v_N(\tan\theta\sin T + \cos T)$ is the initial velocity in the y-direction and v_N is the velocity of the electrons emitted normally to the local surface. The exponential term in the integrand of equation (3) means that it has only a significant contribution for values of y no greater than about a period of the surface, and for this condition, $x(t)$ can be taken as constant. Then since (Gradshteyn et al[15])

$$\int_o^\infty \exp(-ct-bt^2) = \left(\frac{\pi}{4b}\right)^{\frac{1}{2}} \exp\left(\frac{c^2}{4b}\right)\left[\text{erfc}\left(\frac{c^2}{4b}\right)^{\frac{1}{2}}\right]$$

the effective transverse velocity is

$$v_e = v_x(\infty) = ap\left(\frac{E_o \pi e}{2pm}\right)^{\frac{1}{2}} \sin(px_1)\exp\left[\frac{pE_A}{E_o e}(\tan\theta\sin T + \cos T)^2\right]$$

$$\times \left[\text{erfc}\left\{\left(\frac{pE_A}{E_o e}\right)^{\frac{1}{2}}(\tan\theta\sin T+\cos T)\right\}\right] + \left(\frac{2E_A}{m}\right)^{\frac{1}{2}}(\cos T\tan\theta-\sin T) \tag{5}$$

The mean transverse energy is then:

$$\bar{E}_T = \int_o^{2\pi/p}\int_{-\pi/2}^{\pi/2} E_T(\theta,x_1)N(\theta)d\theta dx_1 \left[\int_o^{2\pi/p}\int_{-\pi/2}^{\pi/2} N(\theta)d\theta dx_1\right]^{-1} \tag{6}$$

where $E_T(\theta,x) = mv_e^2/2$ and an intrinsically narrow distribution is assumed by using $N(\theta)$ given by equation (2).

Since the limiting resolution is insensitive to the form of the angular distribution and a function of only the mean transverse energy, equation (1) was used to calculate the limiting resolution as a function of electric field, spacing and MTEE, calculated from equations (5) and (6) for various sinusoidal

4.8

surfaces. The results are shown in Figure 3, where lines of constant transverse energy, determined from equation (1) are also plotted.

When the slope effect, i.e. the first term of equation (3), is dominant the approximation $x(t) = x_1$ is irrelevant. However, if the field distortion effect dominates, i.e. the second term, then for period-to-amplitude ratios less than about ten, the transverse displacement of electrons is such that the approximation $x(t) = x_1$ within the distorted field region is no longer valid, and for this region (field distortion effect greater than 10% of the total mean transverse energy) the curves in Figure 3 are shown as dotted lines.
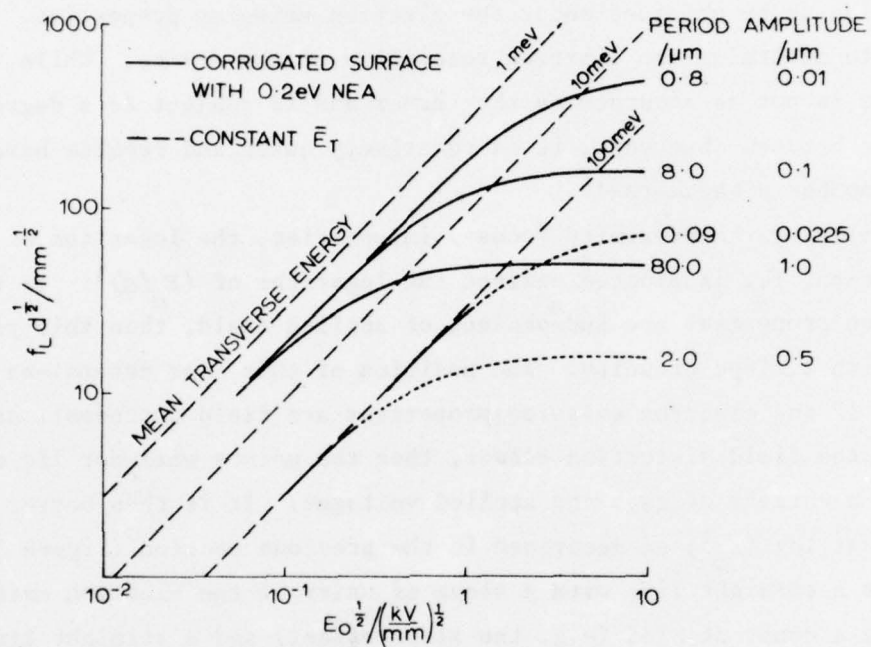
FIGURE 3. The calculated dependence of $f_L(d)^{\frac{1}{2}}$ on $E_o^{\frac{1}{2}}$ for photocathodes with Gaussian emission distributions about the local normal in proximity tubes.

Two limiting case regions are apparent:

(a) At low fields the slope effect dominates and the transverse energy is a constant. Here the term due to the initial velocity in equation (3) dominates and $v_e = v_N(\cos T \tan\theta - \sin T)$. Thus the MTEE depends only on the ratio of period to amplitude for the corrugated surface and not on its scale. In addition, $f_L(d)^{\frac{1}{2}} \propto (E_o)^{\frac{1}{2}}$ for a particular surface.

(b) At high electric fields the field effect dominates and the MTEE increases with field, so that $f_L(d)^{\frac{1}{2}}$ is constant for a given surface. In equation (5) the

term due to the initial velocity becomes small and both the exponential and the error function are independent of E_o giving:

$$v_e = aps\sin(px_1)(\pi eE_o/2pm)^{\frac{1}{2}}$$

Thus the MTEE depends on both the period-to-amplitude ratio and the period of the corrugations, and is proportional to E_o.

4.   RESOLUTIONS MEASUREMENTS ON PROXIMITY TUBES

A measurement of the MTF of a proximity focused image intensifier as a function of both the applied voltage and the photocathode-to-phosphor gap, d, allows information to be obtained about the electron emission properties. The alternative is to determine the limiting resolution of the device. While the latter technique is not as accurate as the former and is subject to a degree of systematic error between observers, it is relatively quick and results have been published by a number of authors[5,6].

Conventionally, for a proximity focused intensifier, the logarithm of the limiting resolution, f_L, is plotted against the logarithm of $(E_o/d)^{\frac{1}{2}}$. If the electron emission properties are independent of applied field, then this yields a straight line with a slope of unity. The position of this line determines the MTEE. However, if the electron emission properties are field dependent, as would be the case for the field distortion effect, then the points will not lie on a single line for a variety of gaps and applied voltages. It is then better to plot $\log (f_L d^{\frac{1}{2}})$ against $\log (E_o^{\frac{1}{2}})$ as described in the previous section (Figure 3). This plot yields a straight line with a slope of unity if the electron emission is characterised by a constant MTEE (e.g. the slope effect) and a straight line with zero slope if field distortion limits the attainable resolution.

Measurements of limiting resolution reported by previous authors are plotted in Figure 4. The RCA data are from Fisher et al[6] and were obtained on a $GaAs/Ga_xAs_{1-x}P/GaP$ photocathode structure. The data from this laboratory[5] are on (111)B $GaAs/Ga_xAl_{1-x}As/GaP$ samples.

It is apparent that for the range of gaps and applied voltages used, the dependence of limiting resolution on these parameters does not fit the field distortion model. Instead the data fit a constant MTEE, $\bar{E}_T$, with this energy equal to 148 ±15 meV for the RCA data, and 107 ±18 meV for our data. This implies that these high values of $\bar{E}_T$ should also apply at much lower electric fields, and in particular should be observed using LEED equipment.

5.   MEASUREMENTS OF TRANSVERSE ENERGY AT LOW FIELDS

5.1 Introduction

The hemispherical grid and phosphor assembly of a commercially available

LEED system offers a convenient method of displaying the angular distribution of electrons with energies of about 100 eV emitted or reflected from a source. The same apparatus has been used to measure the angular distribution of photoelectrons from a GaAs photocathode[2], and if the NEA is known the corresponding distribution of transverse velocities can readily be derived. In our experience the direct interpretation of the displayed distribution may be subject to error caused by electric fields in the region usually assumed to be field free. This effect is negligible for 100 eV electrons but is important when their energy is as low as 0.1 - 0.2 eV.
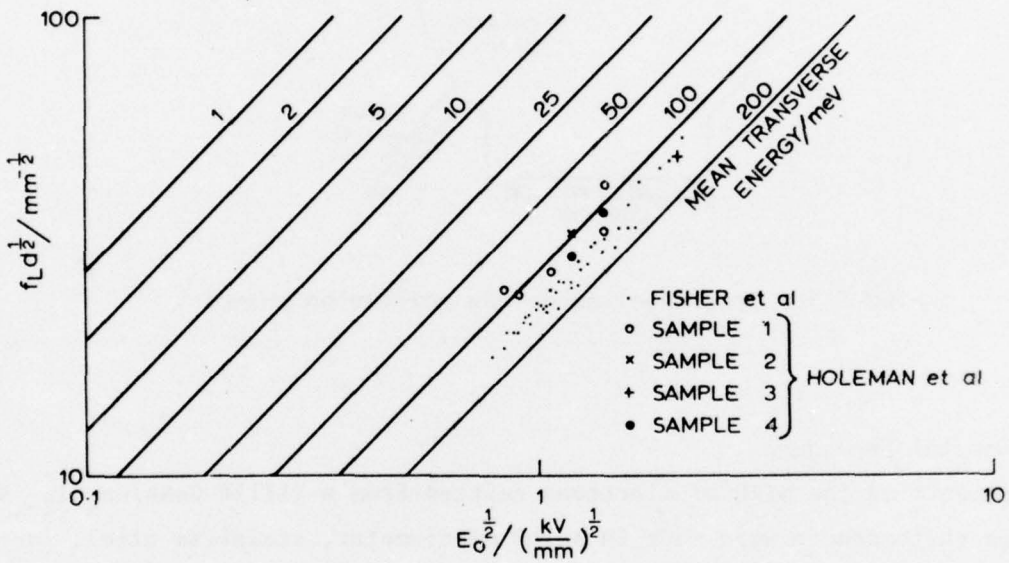
FIGURE 4. The measured dependence of $f_L(d)^{\frac{1}{2}}$ on $E_o^{\frac{1}{2}}$ for proximity tubes.

There were two main sources for the stray electric fields causing the effect: (a) Work function variations across the photocathode surface, and differences between the work function of the photocathode and that of its immediate support, produce significant electric fields in the space close to the emitting surface. This effect has previously been suggested by Burns[16].
(b) If the photocathode and first grid are not accurately at the same potential (including differences in work function) a field is created which does not have the radial symmetry necessary to preserve the original angular distribution. The

equipotentials are planar immediately adjacent to the photocathode surface and
hemispherical near the first grid.

In this section the experimental evidence for these effects is discussed and a
measurement of MTEE at applied electric fields as low as 2 V mm^{-1} is described, the
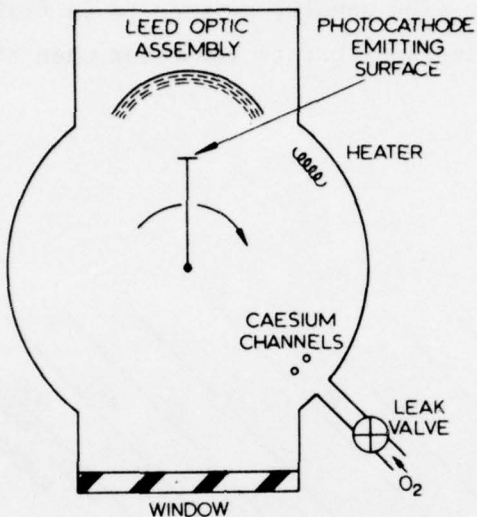effect of the errors being minimised.

FIGURE 5. Cross section of the activation chamber.

5.2 *Experimental Procedure*

Measurements of the MTEE of electrons emitted from a (111)B GaAs/Ga$_x$Al$_{1-x}$As/GaP
transmission photocathode were made in a 250 mm diameter, stainless steel, ion-
pumped vacuum chamber at a background pressure of 10^{-8} Pa. The photocathode was
cleaned by heating near the congruent evaporation temperature using radiation from
a hot rhenium filament mounted in the vacuum chamber. The photoemission was
maximised by exposing the clean gallium arsenide surface to caesium from a caesium
chromate source, and to oxygen admitted via a leak valve. The chamber layout is
shown schematically in Figure 5, whilst the sample holder, designed to minimize
the effects described in Section 5.1(a), appears in Figure 6. By removing all ion
pump magnets from the vacuum system during measurements, magnetic field components
normal to the cathode surface were reduced to less than 10^{-4} Wb m^{-2}. At this level
magnetic focusing is insignificant.

The LEED system was operated with the grid assembly at earth potential and
a variable voltage, $-V_{col}$, applied to the photocathode. The distribution
displayed on the phosphor screen showed a smooth monotonic decrease in intensity
with distance from a single central maximum and except at the lowest collection
voltages, it exhibited circular symmetry. For simplicity, a measurement method

4.12

was chosen which determined the half width of the distribution at the half maximum electron intensity points. Two photographs of the phosphor were taken at each value of V_{col}, one with 10^{-3} lumen photocathode illumination and the other with 0.5×10^{-3} lumen at the same colour temperature (2854K) and the same illuminated area (about 1 mm diam.) The half width of the distribution on the first photograph was then measured at a density equal to the peak density on the second photograph. The corresponding apparent angle of emission $\Psi_{\frac{1}{2}}$, relative to the photocathode normal, is defined by assuming that the electron has travelled radially from its point of emission at the centre of the grids.
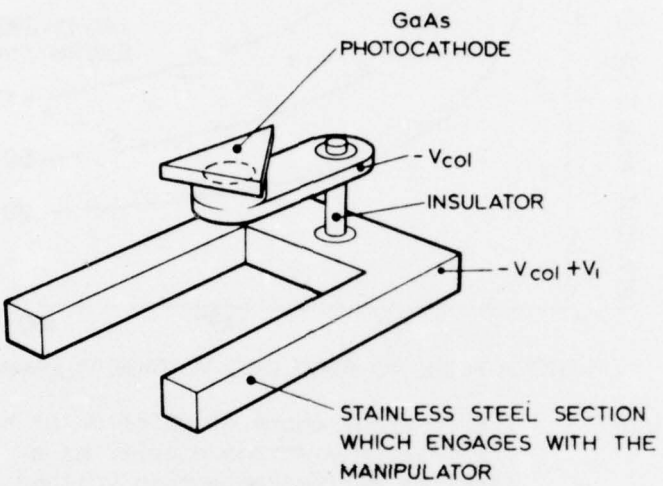
FIGURE 6. Sample holder.

Typical results are shown in Figure 7. $\Psi_{\frac{1}{2}}$ is a strong function of V_{col} and reaches a maximum of about 6° when V_{col} is about 15 V. When V_{col} was less than 4 V no electrons reached the phosphor. When $4 < V_{col} < 15$ V the apparent angle of emission increased rapidly with V_{col}, the spot on the phosphor had the triangular shape of the cathode, and the relative motion of the light spot on the cathode and the image on the phosphor were out of phase. At $V_{col} > 15$ V the apparent angle diminished with increasing V_{col}, the image became circular and the relative motions were in phase. The values of V_{col} at which these characteristic features appeared, depended on the bias voltage V_1 applied to the isolated part of the sample holder, with respect to the photocathode. The maximum moved to higher V_{col} for negative V_1 and to lower V_{col} for positive V_1, whilst observable changes occurred for changes in V_1 of the order of 1 volt. For the measurements shown in Figure 7, V_1 was held at +1 V.

4.13

None of these effects would have occurred if the electrons had been moving in an effectively radial field, except the failure of the electrons to land at voltages below a particular value of V_{col}. Since this radial field condition is normally assumed, and leads to equivalence of initial and apparent emission angles, it is important to understand the effects more fully if transverse emission energies are to be measured with confidence.
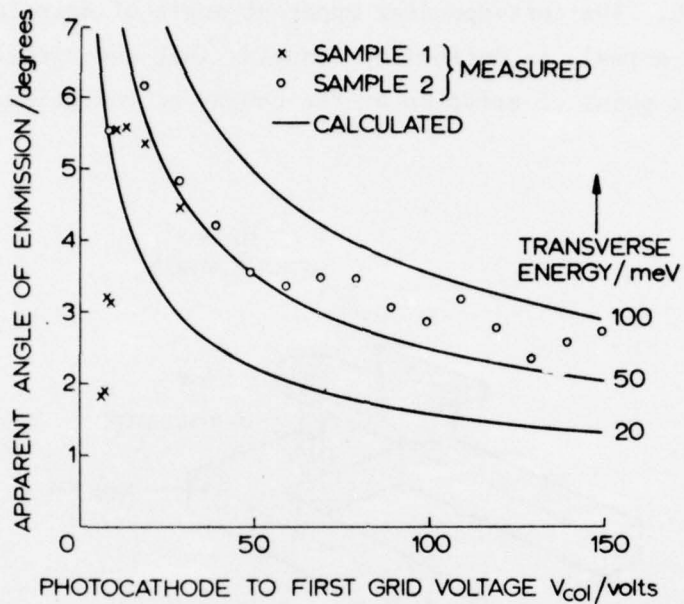

FIGURE 7. The apparent angle of emission at half the maximum electron density as a function of the collection voltage.

5.3 Investigation of Stray Fields in the LEED Optic Assembly

The series of current-voltage curves in Figure 8 were obtained for $0 < V_{col} < 12$ V, as a function of V_1, using the grid and phosphor assembly as a collector. An apparent difference in work function, $\Delta\phi_a$, between the cathode and collector of $\simeq 12$ V was obtained when V_1 was zero. $\Delta\phi_a$ diminished as V_1 was increased, saturating at large V_1 to a minimum of 2.6 ±0.2 V, a more realistic value for the work function difference $\Delta\phi$. For a particular value of V_1, the current began to fall at approximately the value of V_{col} at which the apparent emission angle reached a maximum.

The measurements indicated that electric fields small enough to be produced by differences in work function could have a marked effect on the electron trajectories, and suggested that such differences may be the cause of the anomalous behaviour described in Section 5.2. This possibility was investigated using a resistance paper* analogue method. Initial trials showed that

* Sensitised Coatings Limited, Redlands, Coulsdon, Surrey.

4.14

if the sample was mounted a distance in front of the holder, as is the case for the configuration shown in Figure 6, then the effect of work function differences between the photocathode and its holder was substantially reduced. However, there remained the work function differences between activated and unactivated parts of the sample itself. Therefore in a further simulation, the sides and rear of the cathode were arbitrarily biased -3 V with respect to the front surface, and the potential distribution in front of the cathode was determined as a function of the effective accelerating potential difference, V_{ACC}, where $V_{ACC} = V_{col} - \Delta\phi$.
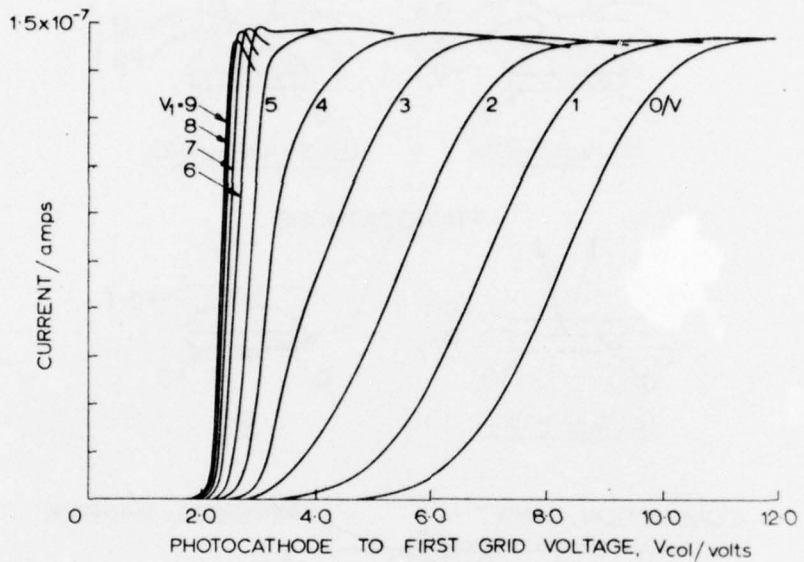
FIGURE 8. Measured current-voltage characteristics of the photocathode and LEED optics assembly as a function of V_1.

It became apparent that at low accelerating voltages (Figure 9a) a potential barrier existed in front of the cathode which would prevent electrons from escaping to the collector. At higher accelerating voltages ($\approx$ 3V), Figure 9b, the potential barrier was penetrated along the axis of symmetry and a small region with the shape of the cathode was produced through which electrons could escape, giving collector current. This aperture would determine the size and shape of the image on the phosphor and it could also produce the reverse motion of the light spot on the photocathode compared to the image on the phosphor as shown in Figure 9d. The particular value of V_{ACC} at which these effects appeared was controlled by the negative bias on the rear surface of the photocathode, corresponding to the difference in work function between its front and rear surfaces. As V_{ACC} was further increased, Figure 9c, this region was enlarged and the focusing effect would be reduced until at $V_{ACC} > 15$ V none of the electrons would experience a retarding potential during its transit to the screen. It is

4.15

also clear why erroneously high values of $\Delta\phi_a$ greater than $\Delta\phi$ were obtained from the current-voltage curves when V_1 was small. The potential energy diagram in Figure 9e shows that a large collection voltage was necessary in order to reduce the maximum of the potential barrier to below the bottom of the conduction band in the bulk of the gallium arsenide. The role of V_1 was to partially cancel the potential barrier in front of the cathode without the need to increase V_{col}.
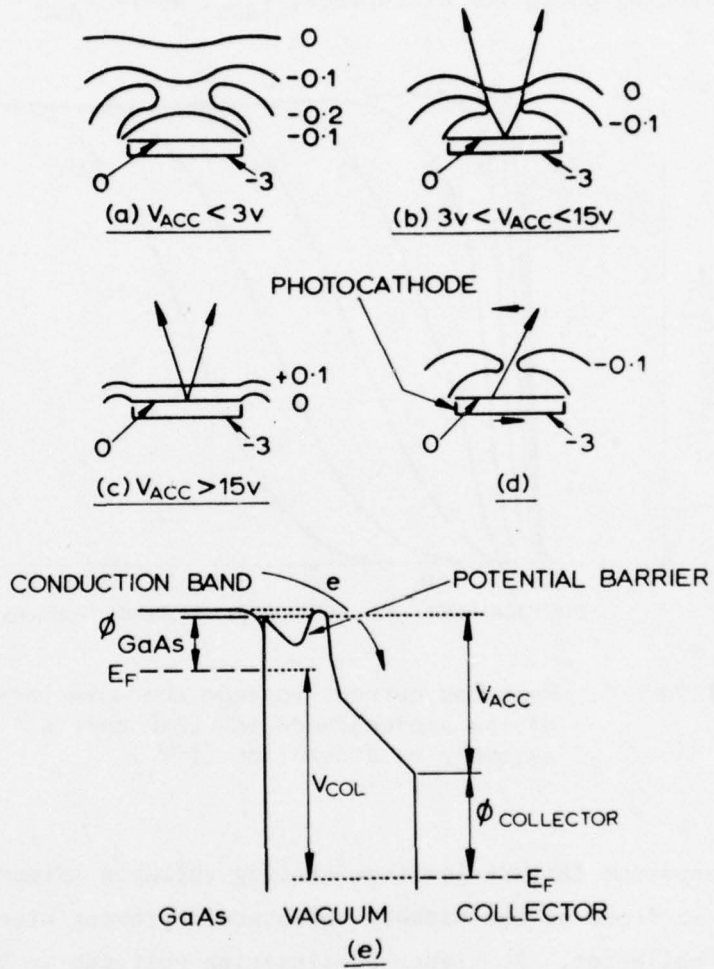

FIGURE 9. (a)(b)(c) The equipotentials in front of the cathode.
The voltages are referred to the cathode.
(d) The reverse motions of the illuminating spot and image on the phosphor.
(e) The potential energy versus distance for an electron.

Thus a number of the anomalies observed in Section 5.2 can be qualitatively explained in terms of the stray electric fields resulting from work function differences. Even if a suitable design removes the effect of the sample holder work function, serious distortion of the electron trajectories can be introduced

by the unactivated parts of the photocathode. Therefore it is unlikely that the degree of distortion will be calculable.

By working at higher values of V_{col} this effect should become negligible and then $\Psi_{\frac{1}{2}}$ should become independent of V_{col}. However it is apparent from Figure 7 that this is not the case, and the second mechanism introduced in Section 5.1 (b) must be considered. Unlike the previous mechanism, the effects produced can now be calculated. Lamport[17] has used numerical methods to compute the trajectories of 0.2 eV electrons in a LEED apparatus with a flat conducting source.
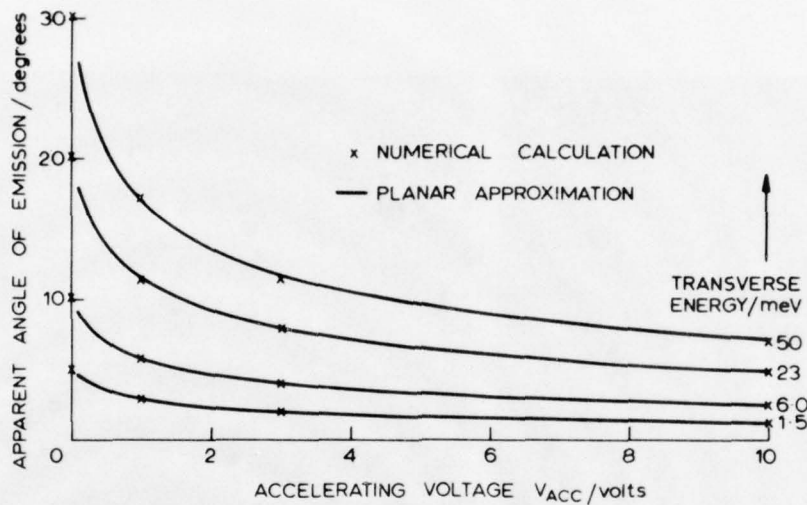
FIGURE 10. The apparent angle of emission of electrons with 0.2 eV emission energy.

The results are shown in Figure 10, from which it is apparent that the initial angular distribution is severely distorted by accelerating voltages as low as 0.5 V. Alternatively the distortion can be determined by approximating the hemispherical geometry with a planar one, in which case the apparent angle of emission corresponding to a given E_T is

$$\Psi = \tan^{-1}\left[\{(E_A + eV_{ACC})^{\frac{1}{2}} - (E_A)^{\frac{1}{2}}\}2(E_T)^{\frac{1}{2}}/eV_{ACC}\right]$$

The results of this calculation are compared with those of Lamport[17] in Figure 10. Since the agreement is good and is not expected to deteriorate at higher voltages this convenient analytical approach was applied over the range of accelerating voltages used experimentally, and the calculated curves fitted in Figure 7, to the measured values of $\Psi_{\frac{1}{2}}$ vs V_{col}. This gave a value for the transverse energy corresponding to $\Psi_{\frac{1}{2}}$, $E_{T\frac{1}{2}}$, of 70 ±20 meV for 75 V < V_{col} < 150 V, corresponding to

an applied field between 1.3 and 2.7 V mm^{-1}. In order to calculate the MTEE, $\bar{E}_T$, it was assumed, as in Section 4, that the electron density distribution on the phosphor was Gaussian, for which
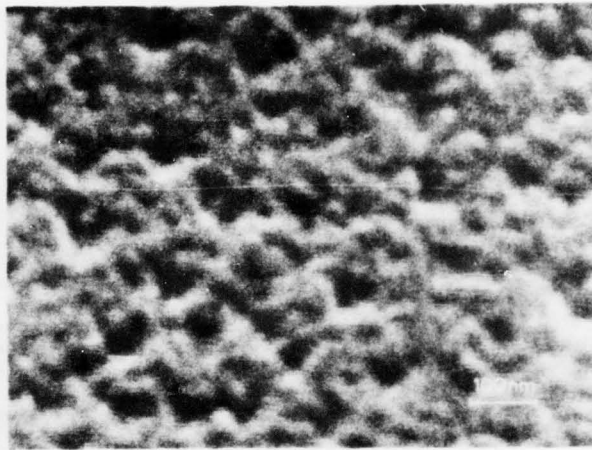
$$E_{T\frac{1}{2}} = (-\ln 0.5)\ \bar{E}_T$$

This yields a value of 101 $\pm$29 meV for $\bar{E}_T$ at applied fields $\approx$2 V mm^{-1}.

The photocathode reflection sensitivity during these measurements was of the order of 500μA lm^{-1} giving 100μA lm^{-1} in transmission for the photocathode gallium arsenide layer thickness of these samples. It was found that as the cathode sensitivity dropped, the MTEE decreased.
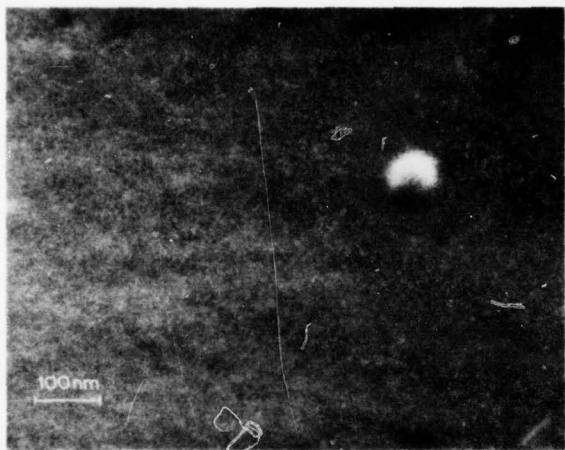
(a)   (b)

FIGURE 11. Scanning electron micrographs of a pair
of photocathode samples. (Tilt angle 45°).
(a) An as-grown surface.
(b) A heat-cleaned surface.

6. SCANNING ELECTRON MICROSCOPE INVESTIGATIONS

The photocathode surfaces have been examined using a scanning electron microscope (SEM)* in the secondary emission mode. For each observation a photo-cathode structure was broken to provide both a control and a sample which was heat cleaned in the LEED apparatus before its transfer in air to the SEM. The temp-erature of the heat treatment was that used in the determination of the MTEE and corresponded to that which gave the maximum photoemission sensitivity. Although

* Phillips PSEM 500.

its absolute value was not accurately known, it was in the region of 600°C and samples so heated did not show the visible film associated with surface decomposition. Figure 11 shows a scanning electron micrograph for a typical sample pair. At (a) the as-grown control sample exhibits a surface largely devoid of structure down to the measured resolution limit of 10 nm. The sample at (b) however, which has been heated for 30 minutes without subsequent exposure to caesium, has undergone a marked change. A surface structure has developed with features ranging in size from 20 to 100 nm and with the larger of these appearing as triangular pits with a common orientation. Whilst the indices of the crystal planes forming the pit sides have not been established, previous work on facetting[12,18] has shown that (110) planes are developed and it is probable that this is also the case here.

7. DISCUSSION

The measured MTEE of 101 ±29 meV at 2 V mm^{-1} for a GaAs/Ga$_x$Al$_{1-x}$As/GaP photocathode (Section 5) is in good agreement with 107 ±18 meV measured on similar photocathodes at fields of 1000-4000 V mm^{-1} in proximity focused image tubes (Section 4). Although there may be systematic errors introduced by the assumption of a Gaussian distribution in Sections 4 and 5 it is expected that these will be small compared with the hundredfold discrepancy outlined in Section 1. It is apparent therefore that these results largely remove the disagreement between the measurements of MTEE in image tubes and in a LEED apparatus[2]. We have considered reasons for the difference between these sets of low field data and suggest two main possibilities: firstly, our work used heat-cleaned surfaces which were similar to those used in the proximity tubes and which were known to be facetted, whereas Pollard's work[2] used ion bombarded surfaces which were facet free. Secondly, we have shown that serious errors can arise when a LEED apparatus is used with very low energy electrons. The direct interpretation of the low field measurements in this paper would have given transverse energies of about 1-2 meV.

The MTEE which we have measured is about two orders higher than that predicted by the theory of the emission process and is independent of the applied electric field between 2 V mm^{-1} and 4000 V mm^{-1}. It is interesting to consider this problem in the light of the rough surface model developed in Section 3. The field independence indicates that the field distortion effect is insignificant and suggests that the slope effect is dominant. The calculated MTEE in Figure 3 shows that if an NEA of 200 meV is assumed, the measured MTEE would be given by surface corrugations with a period-to-amplitude ratio of approximately four, corresponding to surface angles (T, Figure 2) of up to 45°. Furthermore, the slope effect produces a transverse energy proportional to the NEA, qualitatively

confirmed by the observation in Section 5 that the MTEE decreased as the sensitivity decayed. The absence of a field dependent MTEE at the highest applied electric field sets an upper bound of about 100 nm to the period of the corrugations producing this high transverse energy, whilst periods less than the wavelength of the emitted electron can be expected to have little effect. This sets a lower bound of about 2.5 nm.

This range of periods encompasses the size of the features visible in Figure 11, whilst the surface angles may be compared with the expected value of 35° for (110) facets on a (111)B surface. There is satisfactory agreement if the uncertainty in the NEA and the limitations of the model are accepted, and we believe that this structure is a very probable cause of the high transverse energy. On the other hand the much larger scale structure normally detected by optical microscopy and resulting from the method of growth cannot be responsible.

8. CONCLUSIONS

In proximity focused image intensifiers, gallium arsenide photocathodes give a resolution similar to that for multialkali devices and in contrast to the improvement predicted by theory for an NEA emitter. This corresponds to a mean transverse emission energy in the tube of 100 meV which is approximately two orders higher than expected, and is comparable to the value measured at near zero applied electric field in a LEED system.

An angular structure not resolvable by optical microscopy has been detected on the surface of the photocathode by scanning electron microscopy and calculations show that this can provide an explanation for the major features of the anomaly. It has been demonstrated that the structure is a direct result of the heat cleaning which forms part of the photocathode activation process. Thus the resolution achievable with current gallium arsenide photocathodes may not represent a fundamental limitation if changes in the activation procedures can significantly reduce the transverse emission energy.

ACKNOWLEDGEMENTS

REFERENCES

1. BURT, M.G., *personal communication*, 1975.
2. POLLARD, J.H., *8th Army Sci. Conf.*, West Point, New York, (unpublished) 1972.

3. BELL, R.L., *Negative Electron Affinity Devices*, (Oxford: Clarendon Press), 1973, pp 128-9.

4. PIAGET, C., POLAERT, R., RICHARD, J.C., *Proc. 6th Symp. Photoelectronic Image Devices (to be published in Advan. Electron. Electron Phys.)* 1974.

5. HOLEMAN, B.R., CONDER, P.C. and SKINGSLEY, J.D., *Proc. 6th Symp. Photoelectronic Image Devices (to be published in Advan. Electron. Electron Phys.)*, 1974.

6. FISHER, D.G. and MARTINELLI, R.U., *Advances in Image Pickup and Display*, Vol. 1, ed. B Kazan (London: Academic Press), 1974, pp 71-162.

7. MARTINELLI, R.U., *Appl. Optics*, Vol. 12, 1973, pp 1841-5.

8. JAMES, L.W., *personal communication*, 1974.

9. NEEDHAM, M.J. and THUMWOOD, R.F., *Advan. Electron. Electron Phys.*, Vol. 28A, 1969, pp 129-36.

10. HSIEH, J.J., *J. Crys. Growth*, Vol. 27, 1974, pp 49-62.

11. ASTLES, M.G. and ROWLAND, M.C., *J. Crys. Growth*, Vol. 27, 1974, pp 142-7.

12. MACRAE, A.U., *Surface Sci.*, Vol. 4, 1966, pp 247-64.

13. RUSSELL, G.J., IP, H.K. and HANEMAN, D., *J. Appl. Phys.*, Vol. 37, 1966, pp 3328-30.

14. KLOPFENSTEIN, R.W. and WEHNER, R.K., *R.C.A. Rev.*, Vol. 34, 1973, pp 630-54.

15. GRADSHTEYN, I.S. and RYZHIK, I.M., *Table of Integrals, Series and Products*, (Academic Press), 1965, p 307.

16. BURNS, J., *Final report U.S. Army contract DA-44-009-ENG-5004*, 1965.

17. LAMPORT, D.L., *personal communication*, 1973.

18. CHEN, J.M., *Surface Sci.*, Vol. 25, 1971, pp 305-14.

A SIMPLE DETERMINATION OF THE ENERGY LOSS PROFILE

FOR ELECTRONS IN A SEMI-INFINITE MEDIUM

D. J. Day

ABSTRACT

A procedure is described for predicting electron energy loss profiles (dose-depth curves) in any semi-infinite material for incident electrons in the kilovolt to megavolt energy range.

A SIMPLE DETERMINATION OF THE ENERGY LOSS PROFILE
FOR ELECTRONS IN A SEMI-INFINITE MEDIUM

D. J. Day

INTRODUCTION

In diverse applications of electron beams e.g. welding, X-ray microprobe analysis, solid and gaseous laser excitation, microwave power devices, etc., a criterion for their use is the need for high energy deposition in a predetermined volume. It is important therefore to be able to predict with some confidence the spatial distribution of energy deposition for widely different target materials and electron energies. It is only recently that a universal empirical curve of electron energy deposition (dose-depth curve) has been proposed by Everhart and Hoff[1] based on direct measurement in silicon and air. In this paper we adopt scaling laws observed by Everhart and Hoff to obtain a simplified theoretical description of electron energy loss. This predicts electron energy deposition on any semi-infinite solid, liquid, or gas for the kilovolt to megavolt electron energy range. Its prediction is specific to the material and electron energy of interest.

THEORETICAL AND EMPIRICAL FOUNDATION

Scattering of an energetic electron by an atom can be described by the probabilities of small angle elastic scattering (nuclear collisions) and large angle inelastic scattering (electronic collisions), which are determined by the form of the atom's interaction potential and the electronic and vibrational excitation processes available to it. Even after many scattering events in a random scattering process, the energy dissipation and distribution of electrons is defined uniquely by these single scattering parameters, provided of course that the target's dimensions do not interfere with the scattering process.

This can be demonstrated by considering elastic scattering by a power law potential of a screened nucleus

$$V(r) = \frac{Ze^2 a^{s-1}}{s r^s} \tag{1}$$

where $a = 0.8853 \, a_o Z^{-1/3}$ is the effective screened radius of the atom with a_o the Bohr radius, Z the atomic number and s the power law exponent. Which leads to a simple differential scattering cross section

$$d\sigma = \frac{\pi}{2}\left[b^2 a^{2s-2} \frac{(3s-1)}{8s^2}\right]^{1/s} \left(\frac{T_m}{T}\right)^{1+(1/s)} \frac{dT}{T_m} \tag{2}$$

where b is the collision diameter Ze^2/E, T the energy transfer and T_m its maximum value given by

$$T_m = \frac{4AE}{(1+A)^2} = \mu E \tag{3}$$

with A the mass of the scattering particle in units of the mass of the scattered particle. Lindhard[2] and Baroody[3] have shown that all moments of the distribution of scattered particles at rest are determined uniquely by s, A and the initial energy E. In particular the average path length L becomes

$$L = \frac{(s-1)}{N\pi\mu} \left[\frac{8s^2}{(3s-1)}\right]^{1/s} \frac{E^{2/s}}{(Z^2e^4a^{2s-2})^{1/s}} \tag{4}$$

That is to say, if the power law s of the interaction potential and the average path length L were known for any electron energy E then the mass ratio A (i.e. μ) and all moments of the electron distribution are determined uniquely at that energy.

Elastic collisions can therefore be described quite simply. Inelastic collisions are not so amenable to precise description. The Bethe theory of stopping power approximates inelastic loss as a continuous slowing down process between elastic collisions i.e. a viscous drag. Bethe's equation for energy loss is

$$-\frac{dE}{dl} = \frac{2\pi NZe^4}{E} \, ln\left(\frac{uE}{I}\right) \tag{5}$$

where I is defined as a mean excitation energy of inelastic losses along a path l, and u is a constant with a value of 1.16. This theory is valid for high energy electrons where $E \gg I$, but would appear a coarse approximation as $E \rightarrow I$. The Bethe energy loss range R_B is defined as

$$R_B = \int_E^O \frac{dE}{dE/dl} = K \int_0^\epsilon \frac{\epsilon d\epsilon}{ln \, \epsilon} \tag{6}$$

where $K = 9.4 \times 10^{-12} I^2 A/Z$ g/cm , and the incident energy to ionisation energy ratio $\epsilon = u \, E/I$. This range describes the average distance travelled by an electron in losing its energy. Berger and Seltzer[4] have evaluated this integral for representative materials and electron energies. Their results can be fitted by a power law of the form

$$R_B = KBE^n \tag{7}$$

with B and the exponent n taking different-best fit values over various ranges of ϵ. Everhart and Hoff[1] have defined such power laws for the Bethe range as (see Figure 1)

$$R_B/K = \begin{cases} 0.95\epsilon^{1.51} & 5<\epsilon<50 \\ 0.68\epsilon^{1.62} & 10<\epsilon<100 \\ 0.34\epsilon^{1.78} & 50<\epsilon<500 \end{cases} \tag{7A}$$
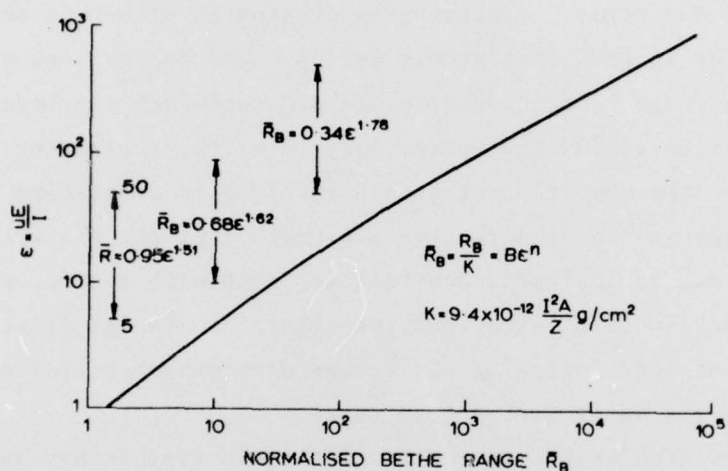

FIGURE 1.   Universal curve of normalised Bethe range
for normalised electron energy (after
Everhart and Hoff[1])

The major problem is how to combine elastic and inelastic processes in a unified theory. This has been achieved in a rather ad hoc basis in Monte Carlo computer simulations[5] of scattering phenomena. More precise calculations based on statistical transport theory have been given by Spencer[6]. Good agreement is found for these calculations with experimentally determined dose-depth curves[1,7]. Unfortunately these computational techniques are difficult to interpret in a physical sense and offer little guide for extrapolation to a general case.

Everhart and Hoff[1] however have offered an empirical universal dose-depth curve, normalised to the Bethe range, based on the observation that all available data exhibit good scaling properties with the Bethe range, provided $E>I$. From their own appreciation it is clear that a single universal curve is not expected,

since the contribution from high angle scattering will increase with target mass. What is significant in their observation is that scaling to the Bethe range not only holds for a wide range of mass number for the target, but also for considerably lower electron energies in the kilovolt range than has hitherto been considered its lower bound of approximation.

HYPOTHESIS

If we accept the scaling properties of the total energy loss to the Bethe range, this allows an alternative view of the complex scattering processes of high and low angle scattering of both primary and secondary electrons.

All energy from the primary electrons is dissipated either in exciting secondary electrons or in producing atomic motion. The energy loss profile there-fore describes the average generation rate of both secondary electrons at rest and of atomic motion. If we follow the energy loss in a real scattering sequence of an incident electron, the number of electrons involved in describing the dissipation of the incident energy is non-conservative i.e. each incident particle generates on average n electrons due to inelastic scatterings, each with average energy loss I. After considering many incident electrons, we obtain an average distribution of secondary electrons at rest following the energy dissipation histories, which is observed to scale to the Bethe energy-loss range.

It is an obvious step to try to replace inelastic scattering, where the number of electrons are not conserved, by an elastic scattering process, where the number of electrons are conserved. This will require an adjustable parameter, or parameters, to meet all known boundary conditions of the process.

Consider elastic scattering by a power law potential (discussed in the previous section) for which the average path length L is given by equation (4). To satisfy the Everhart and Hoff scaling laws we require this to be equivalent to the Bethe energy-loss range. The power law approximation to the Bethe range, given by equation (7) immediately yields the necessary conditions for this equivalence as

$$n \equiv \frac{2}{s} \tag{8}$$

and

$$\mu \equiv 2(s-1)\left(\frac{8s^2}{3s-1}\right)^{1/s} \frac{Z^{(5s-8)/3s}}{B}\left(\frac{1281}{I^2}\right)^{1-(1/s)} \tag{9}$$

An effective mass A of the scattering centre can therefore be deduced from μ through equation (3). The adjustability of A reflects the facts that the average mass for all collisions is not the mass of the target nucleus and that the energy dissipated in atomic motion is now due to the energetic secondary electrons, all of

5.6

which have the energy of the incident electrons; the effective mass will therefore be less than the true mass.

With the power law s, the mass ratio A and the incident energy E defined uniquely, all moments of the resultant distribution of rest particles are also determined uniquely. Baroody[3] has discussed scattering by power law potentials and shown that for light screening i.e. $s \sim 1$, which is a reasonable approximation for the Bethe range since $n \sim 2$, the moments of the distribution of stationary particles have a very simple functional form. For a Gaussian approximation to the distribution of secondary electrons, the projected range R_p which determines the peak of the Gaussian distribution and its variance μ_2 becomes

$$\frac{R_p}{R_B} = \frac{1}{(1+As/4)} \qquad \text{for } s \sim 1 \tag{10}$$

and

$$\frac{\mu_2}{R_B^2} = \frac{1}{(1+As/4)^2} \frac{(As)^2}{4(8+3As)} \qquad \text{for } s \sim 1 \tag{11}$$

For heavy screening, $s > 1$, the expressions for the moments are more complicated, being expressible in the form of incomplete Beta functions.

The total energy loss profile can be determined therefore from only a knowledge of the mean excitation energy I of the target material. The mean excitation energy can in turn be approximated by an empirical formulation attributed to Sternheimer

$$I = (9.76 + 58.8Z^{-1 \cdot 19})Z \tag{12}$$

so that the atomic number Z becomes the only variable to define electron energy loss in any target material provided only that $E > I$.

Therefore, to summarise, for an elemental target the mean excitation energy I can be found from the atomic number and equation (12). From I and the electron energy, the range constants B and n are determined from their variation with ϵ, given in equations (7) and (7A). These constants allow equations (8) and (9) to be evaluated and the effective mass ratio to be found by solving equation (3). This effective mass ratio is then used in equations (10) and (11) to give the range and variance for a Gaussian distribution. For a compound target the mean excitation energy is the sum of losses in the j constituent elements of mass ρ_j

$$\log (I) = \sum_j \frac{Z_j}{A_j} \rho_j \, \log(I_j) \left[\sum_j \frac{Z_j}{A_j} \rho_j \right]^{-1} \tag{13}$$

The effective atomic number is the only other parameter to be averaged such that

$$Z = \sum_j \frac{Z_j \rho_j}{A_j} \left(\sum_j \frac{\rho_j}{A_j} \right)^{-1} \tag{14}$$

RESULTS

In figures (2) and (3) a family of calculated energy loss profiles for targets of different atomic number, but with the electron energy E adjusted to maintain $\epsilon = uE/I \simeq 250$, is compared with consistent data from Spencer[6]. By maintaining ϵ constant the energy dependence of the Bethe range is the same for each curve and only the variation of scattering with atomic number is demonstrated through the family.
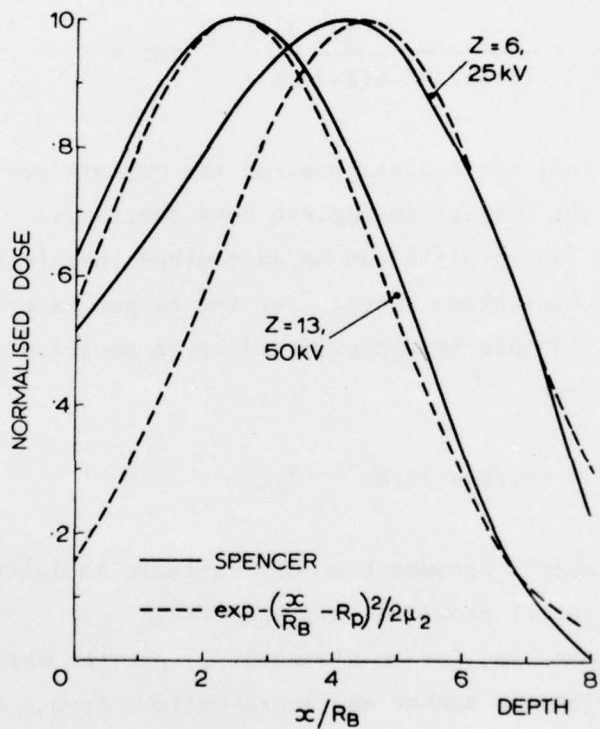
FIGURE 2.   Dose-depth curves for $Z<14$
$$\epsilon \sim 250, \quad \frac{R_B}{K} = 0.34 \, \epsilon^{1 \cdot 78}$$

At low atomic number i.e. $Z<14$, Spencer's data do   not give a good fit to a Gaussian distribution, so that the calculated Gaussian distributions deviate at low penetrations. The calculated range and variance however give excellent agreement with the first two moments of Spencer's distribution and indicate that a better

5.8

approximation might be obtained if higher order moments were included in the distribution i.e. skewness and kurtosis.

At higher atomic number i.e. $Z>14$ Spencer's data do give a good fit to a Gaussian distribution. Again the calculated range and variance give excellent agreement, so that the calculated distributions are very close to those of Spencer.
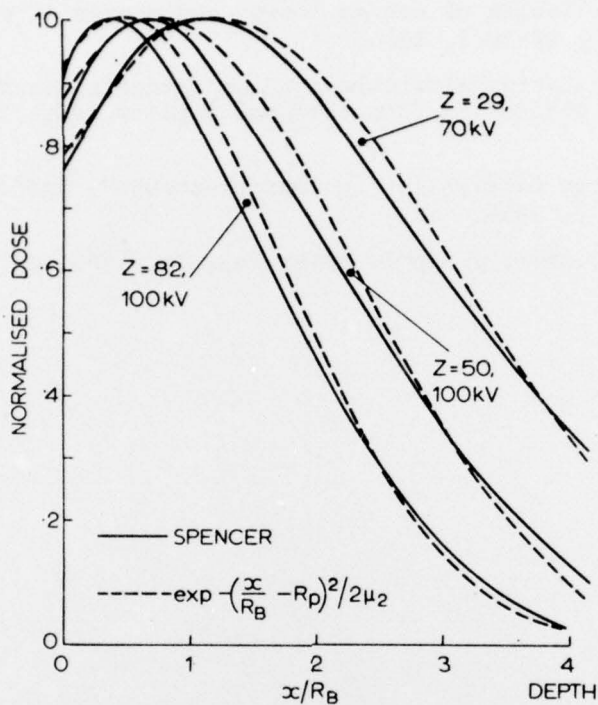
FIGURE 3.   Dose-depth curve for $Z>14$

$$\epsilon \sim 250, \quad \frac{R_B}{K} = 0.34\epsilon^{1.78}$$

CONCLUSIONS

From the well defined properties of elastic scattering at a power-law potential, it has been shown that the requirement for the mean path length of incident electrons to be equal to a power law approximation for the Bethe energy loss range is a sufficient condition to define the effective mass and interaction potential of an equivalent elastic scattering centre. The distribution of scattered electrons at rest derived from scattering by this centre then describes the distribution of secondary electrons at rest and the average atomic motion generated by the electron beam.

ACKNOWLEDGEMENTS

REFERENCES

1. EVERHART and HOFF, *J. Appl. Phys.*, Vol. 42, 1971, pp 5837-5846.

2. LINDHARD, J., SCHARFF, M. and SCHIOTT, H., *K. danske Vidensk, Selsk, Math-fyss. Meddr*, Vol. 33, Nos. 10 and 14, 1963.

3. BAROODY, E.M., *J. Appl. Phys.*, Vol. 36, No. 11, 1965, pp 3565-3573.

4. BERGER and SELTZER, "Tables of energy losses and ranges of electrons and positions", *N.A.S.A.*, SP-3012, 1964.

5. BERGER, M.J., "Monte Carlo Calculations of the penetration and diffusion of fast charged particles", *Methods in Computaticnal Physics*, Vol. 1, Academic Press, New York, 1963.

6. SPENCER, L.V., "Energy Dissipation by fast electrons", *National Bureau of Standards Monograph 1*, 1959.

7. COSSLETT and THOMAS, *Brit. J. Appl. Phys.*, Vol. 16, 1965, pp 779-796.

SERL TECHNICAL JOURNAL

INDEX - 1976

VOLUME 26

*Contributions to recent numbers of the SERL Technical Journal which have
been published elsewhere* ——

The use of confocal unstable resonators in a double Rogowski TEA CO_2 laser.
V. G. Roper, *Optics and Laser Technology, Vol. 8, No. 1, 1976, pp 13-16.*

The thermal imaging response of a pyroelectric target.
B. Turner and H. A. H. Boot, *Infrared Physics, Vol. 16, No. 3, 1976, pp 367-374.*

GaAs reflection photocathodes grown by metal alkyl vapour-phase epitaxy.
M. B. Allenson and S. J. Bass, *Applied Physics Letters, Vol. 28, No. 3, 1976,
pp 113-115.*

A direct-view thermal imaging tube.
H. A. H. Boot, J. G. Castledine, P. G. R. King, K. E. Trezise and B. Turner,
J. of Phys. D (Applied), Vol. 9, No. 5, 1976, pp 679-695.

Isothermal GaAs liquid-phase epitaxy using a rotating substrate technique.
M. G. Astles, J. C. H. Birbeck, C. J. Laversuch and M. C. Rowland, *J. Crystal
Growth, Vol. 34, No. 1, 1976, pp 24-28.*

Device quality epitaxial gallium arsenide grown by the metal alkyl-hydride
technique.
S. J. Bass, *J. Crystal Growth, Vol. 31, 1975, pp 172-178.*

A new semiconductor contact technology.
A. B. J. Sullivan, *Electronics Letters, Vol 12, No. 6, 1976, pp 133-134.*

An electrically tunable narrow band optical filter.
H. A. Tarry, *Electronics Letters, Vol. 11, No. 19, 1975, pp 471-472.*

Papers read at Conferences ——

Reliability of high-frequency silicon IMPATT diodes.
P. Brook and D. J. Taylor, *IEE meeting on reliability of solid state microwave
devices, London, 1975.*

Luminescence efficiency in gallium phosphide.
D. R. Wight, *IPPS conference on materials and processing effects in semiconductor
devices, Brighton, 1976.*

CONTENTS

Closing issue of the SERL Technical Journal.

Editorial.

Recent Technical Journal papers now published
elsewhere or read at conferences.

FILM 3